Universidad de La Laguna

Facultad de Ciencias

Halo mass measurements with the kinetic Sunyaev-Zel'dovich effect

Trabajo Fin de Grado

Autora:
Mónica Natalia Isla Llave

Tutor:
Dr. Carlos Hernández-Monteagudo
(Instituto de Astrofísica de Canarias)

Julio 2022

Agradecimientos

A mi tutor, Carlos, por su increíble paciencia y toda su ayuda,
al Prof.Dr Raúl Angulo por su colaboración en este proyecto,
y a mi familia y amigos por todo su apoyo y cariño.

Resumen

El estudio de la estructura a gran escala del universo es una de las ramas fundamentales de investigación hoy en día en la Cosmología física. Dentro de ella se enmarca la caracterización de cúmulos de galaxias, que son las estructras virializadas más grandes conocidas, así como los modelos de su formación y evolución durante las distintas épocas del universo. Actualmente, se piensa que los cúmulos de galaxias (y todas las zonas sobredensas del universo) tienen su origen en las fluctuaciones primordiales de densidad del universo que crecieron a través de la inestabilidad gravitacional que ocasionan, y que están asociadas a las fluctuaciones cuánticas que crecieron a tamaño macroscópico durante el periodo de inflación. Por lo tanto, conocer las estadísticas de la población de cúmulos de galaxias es una vía para acotar las magnitudes de los parámetros del modelo cosmológico de concordancia.

Parte de las investigaciones en el ámbito de las anisotropías del fondo cósmico de microondas ha aportado una nueva ventana de investigación para cúmulos de galaxias por medio de interacciones entre la radiación de fondo con la materia bariónica. De entre los efectos causados por estas interacciones, este proyecto se fija en el efecto Sunyaev Zel'dovich cinético (kSZ) (Sunyaev and Zeldovich, 1972), que es la distorsión Doppler de la radiación de fondo causada por el scattering Thomson entre los fotones del fondo de microondas y el medio ionizado que se mueve con respecto a él a una velocidad peculiar. Este efecto ha sido utilizado por varias colaboraciones (e.g la colaboración ACTPol (Vavagiakis et al., 2021,Calafut et al., 2021)) recientemente para inferir las masas de gas y totales de cúmulos de galaxias. En ellas se ha observado que se asume que el flujo de kSZ a lo largo de la línea de visión de un cúmulo proviene únicamente del medio intracumular. No obstante, también se espera que haya una contribución a la señal de kSZ por parte del gas ionizado que se mueve con velocidad peculiar fuera del halo. El objetivo de este trabajo es analizar esta contribución proveniente del medio ionizado fuera del tamaño virial de los halos comparándola con la que viene de su interior para halos de distintas masas.

Se han seguido dos métodos para analizar los flujos de kSZ procedentes de los halos, i.e de esferas de radio virial, y de cilindros con apertura el radio virial y profundidad variable: un método semi-analítico, que usa modelos teóricos para caracterizar los campos de sobredensidad y de velocidad peculiar de los cúmulos de galaxias, y otro basado en los datos proporcionados por Prof. Dr. Raúl Angulo de un catálogo de halos y partículas de materia oscura a redshift $z = 0$ obtenidos por medio de una simulación de N-partículas. Para el método semi-analítico se llevó a cabo un desarrollo teórico dentro del marco de la teoría lineal de perturbaciones para modelar el campo de velocidades peculiares y se usó un modelo de sobredensidad de gas que combinaba la contribución de un halo, obtenida por Chaves-Montero et al., 2021, y la contribución de los cúmulos cercanos a la línea de visión que contribuyen al kSZ del cúmulo observado, también llamada contribución a dos halos, obtenida por medio de la función de masa de halos extraída con datos de Ondaro-Mallea et al., 2022 y Tinker et al., 2010. El procedimiento seguido con las simulaciones consistió en elaborar un código que seleccionase las partículas de materia oscura dentro de los volúmenes que se querían observar (esferas de radio virial y cilindros con profundidad variable centrados en los halos) y en comparar los flujos provenientes para cada halo de una población de halos con masas entre 10^{12} y $2 \times 10^{15} M_{\odot}/h$.

Los resultados obtenidos por ambos métodos muestran que para cúmulos de baja masa ($10^{12} - 10^{13} M_{\odot}/h$) la contribución de electrones libres al flujo de kSZ a lo largo de la línea de visión es del $45 - 30\%$ para la profundidad máxima de la línea de visión utilizada de 512 Mpc$/h$. Por otra parte, para cúmulos de mayor masa virial ($\gtrsim 10^{15} M_{\odot}/h$), esta contribución de electrones libres disminuye hasta ser $10 - 5\%$. Los resultados de ambos métodos difieren cuantitativamente en cuanto al crecimiento de la fracción de kSZ proveniente de los halos con la masa del halo, pero esto se podría deber a que los datos de

la simulación de N-partículas utilizada no tienen en cuenta los efectos de la física bariónica, mientras que los perfiles de sobredensidad de Chaves-Montero et al., 2021, sí tienen en cuenta estos efectos. También es posible que se deba a procesos físicos de naturaleza no lineal que afectan a la densidad y velocidad del gas que no quedan fielmente reflejados en nuestro simplificado tratamiento lineal a primer orden de perturbaciones. Se concluye que para masas de halos $\lesssim 10^{13} M_{\odot}$ los resultados apuntan a que la contribución de los electrones fuera del halo supone entre el $30 - 40\%$ del flujo total de kSZ a lo largo de la línea de visión, mientras que para masas $\gtrsim 10^{15} M_{\odot}$ la contribución de los electrones libres cae al $\sim 10\%$. Se planea ampliar estos resultados en el futuro cercano utilizando simulaciones que incluyan materia bariónica.

Abstract

In the past few years, several collaborations studying the Cosmic Microwave Background have used the kinetic Sunyaev-Zel'dovich (kSZ) effect to measure gas mass and total mass of galaxy clusters (Calafut et al., 2021; Vavagiakis et al., 2021). These assume the kSZ signal associated to the galaxy cluster is entirely caused by the ionised gas inside its virial radius, dismissing the kSZ effect caused by unbound electrons that lie next to and along the same line of sight than the clusters'. This would introduce a bias impacting the mass estimates made from kSZ measurements. This project is aimed at quantifying the free-electron contribution to the total kSZ signal along a line of sight towards a galaxy cluster/group characterised by its mass and its redshift. Two methods have been employed: a semi-analytical method, which applies linear theory and uses theoretical models from Chaves-Montero et al. (2021), Tinker et al. (2010), and Vogelsberger et al. (2020); and a numerical method, using data from an N-body simulation at $z = 0$ provided by Prof. Dr. Raúl Angulo. The results obtained from both are qualitatively compatible, with the relative free-electron contribution being greater ($30 - 40\%$) for lower mass halos ($M_{halo} \lesssim 10^{13}$ $M_\odot/h$), and decreasing with mass ($5 - 10\%$ for $M_{halo} \gtrsim 10^{15}$ $M_\odot/h$). The difference between the results obtained with the semi-analytical method and the simulation data, which is primarily seen in the growth curve of the kSZ halo contribution as a function of halo mass, may have been caused by non-linear effects which have been neglected in the linear theory approach this project has followed, although current efforts are investigating more deeply the cause of this mismatch.

Contents

1. Introduction

One of the main goals of Physical Cosmology is making sense of the large-scale structure (LSS) of the Universe. The Universe is currently regarded as being a nearly homogeneous, isotropic large-scale distribution of matter and energy on scales greater than a few hundred megaparsec as part of the Cosmological principle, and being reasonably well described by the Lambda cold dark matter (ΛCDM) model. The deviations from the global cosmic background density are thought to have been originated by small density perturbations in the early Universe, which grew through the gravitational instability they created. The origin of these primordial density fluctuations is thought to reside in the quantum fluctuations which grew to macroscopic proportion during the inflationary phase (according to the GUT this phase transition took place 10^{-36} seconds after the Big Bang). The departures from the mean matter distribution, i.e the presence of overly dense regions, trace the presence of galaxy clusters as it evolves in time. Therefore, the spatial statistics of the galaxy cluster population provide valuable constraints on cosmological parameters. Analysing the mass distribution, as well as the main properties of galaxy clusters and their dependence on redshift is a key task for which it is necessary to have a broad enough set of accurately observed clusters. Over the last decades, multitude of surveys have been conducted in order to map with high precision as many galaxy clusters as possible using different techniques. Those include X-ray observations, which rely on the detection of the hot intra-cluster plasma that fills the cluster potential shaped mostly by dark matter and are limited to nearby objects with moderately high masses. Other surveys have been made using optical and infrared instruments and have managed to trace a high number of galaxy clusters up to $z \sim 1$ redshifts. However, these surveys are often constricted by selection bias factors and instrument sensibilities.

Another observable used to locate and characterise galaxy clusters is the Sunyaev-Zel'dovich (SZ) effect, discovered in 1970 by Rashid Siunyáiev and Yákov Zeldóvich. The non black-body distortion in the Cosmic Microwave background (CMB) due to inverse Compton scattering in the hot plasma is known as the thermal Sunyaev–Zel'dovich (tSZ) effect, whereas the Doppler shift of the CMB radiation by the ionised gas with bulk velocity with respect to the CMB rest-frame is known as the kinetic Sunyaev-Zel'dovich (kSZ) effect (Sunyaev and Zeldovich, 1970, Sunyaev and Zeldovich, 1972). Recent observations made with the *Planck* telescope have been able to confirm the positions of some already known dense clusters and find around 400 new clusters using the SZ effect. The kSZ in particular has been used in the last few years by various collaborations like the ACTPol collaboration (Vavagiakis et al., 2021, Calafut et al., 2021) to infer the masses (gas mass and total mass) of galaxy clusters. A common practice in these collaborations is to assume that the observed kSZ signal from a galaxy cluster comes solely from the ionised gas bound to the cluster, not taking into account the fact that unbound electrons moving with a peculiar velocity with respect to the CMB frame also contribute to the kSZ signal seen along the line-of-sight of the cluster. The aim of this project is to check this assumption to see whether or not the signal associated to a galaxy cluster has a relevant contribution from the unbound electrons in the intergalactic medium, and to quantify it.

This work is organised as follows. Chapter 2 is a summary of some of the key concepts in Physical Cosmology, which are necessary to understand the framework of this project. In Chapter 3 I make an analysis of the halo contribution to the kSZ signal of a galaxy cluster as a function of its mass, as well as its redshift, using a semi-analytical approach; this is to say a series of theoretical models and approximations are used to find the mass and velocity fields around galaxy clusters. Chapter 4 introduces cosmological simulations and the results achieved using data from a N-body simulation through a mock universe with a halo and dark matter particle catalogue at redshift $z = 0$. Chapter 5 discusses the results obtained with both methods and establishes a comparison between them. Chapter 6 contains the final

conclusions and notes on the future work concerning this research topic.

2. Theoretical background

Previamente al desarrollo analítico del problema planteado en la Introducción, conviene hacer un resumen de los conceptos esenciales de cosmología física que se mencionan a lo largo del trabajo. A continuación se hace un breve repaso del modelo de concordancia Lambda-Cold-Dark-Matter (ΛCDM), del modelo jerárquico de formación de estructura a gran escala, del problema de escasez de materia bariónica observada frente a lo que predice el modelo ΛCDM y su extensión en medio intergaláctico caliente, y las posibilidades que ofrecen las observaciones de anisotropías en el fondo cósmico de microondas causadas por interacción de radiación-materia para localizar los bariones restantes, así como para caracterizar los cúmulos de galaxias a distintos redshifts. En este contexto se introduce el efecto Sunyaev Zel'dovich (SZ) en sus dos vertientes: el efecto SZ térmico (tSZ), producido por el scattering Compton inverso de radiación de CMB con gas ionizado a altas temperaturas que se encuentra en cúmulos de galaxias, y el cinético (kSZ), que da lugar a una distorsión por efecto Doppler debido a la velocidad peculiar del medio intergaláctico; ambos resultantes en distorsiones de temperatura de brillo del fondo cósmico de microondas.

The aim of this chapter is to provide the cosmological theoretical basis on which the rest of the project relies, specially the physics surrounding LSS formation and CMB anisotropies. It intends to give a short but scientifically adequate answer to the following question: how and why is the study of the CMB relevant to the study of large scale structure formation and of the missing baryons? At the end, the Sunyaev-Zel'dovich effect will be introduced as a key observable to approach this issue.

2.1 ΛCDM model and LSS formation

The ΛCDM model is the standard model of cosmology, which is a phenomenological model that succeeds at reproducing most cosmological observations. This model consists of a flat Universe undergoing accelerated expansion due to the dark energy component, with a fraction of the total mass-energy density of a flat universe $\Omega_\Lambda = 0.7$ and a matter component with $\Omega_0 = 0.3$, with cold dark matter making up 85% of matter density. Cold dark matter owes the cold part to its velocity being non-relativistic; dark matter is possibly non-baryonic, dissipationless and collisionless (i.e., the dark matter particles interact with each other and other particles only through gravity) and it is a form of matter necessary to account for gravitational effects observed in the LSS of the Universe that cannot be explained by the amount of observed matter. That leaves the baryonic mass-energy portion $\Omega_b \simeq 0.04$, out of which stars and galaxies are made.

The cosmological principle, upon which modern cosmology is based, hypothesises that the Universe is spatially homogeneous and isotropic. However, if this were perfectly true at every scale, there would be no structure formation. It is now thought that tiny primordial density perturbations with respect to the global cosmic background density are most likely due to quantum fluctuations which expanded to macroscopic proportions during the inflationary stage of the Universe. Inflation would have occurred through the breaking of fundamental symmetries, which caused a strongly accelerated expansion. Therefore, the theory of inflation offers an explanation for why the cosmos has a flat geometry and also for the origin of the primordial density fluctuations which gave rise to the LSS. Inflation would also explain the lack of monopoles in the Universe and the "causal horizon" problem, by which far away regions, which may never have been in causal contact, have so-similar properties.

Local deviations from average density and deviations from global cosmic expansion velocity will grow under the influence of the involved gravity perturbations, given density perturbations induce local

differences in gravity. During early evolution, the overdensity will experience a gradually stronger deceleration of its expansion velocity and will attract matter so the slowing-down of the initial cosmic expansion gets correspondingly stronger. Once the perturbation reaches over-density and leaves the linear regime ($\delta\rho/\rho \sim 1$), it starts to form a gravitationally bound object. The matter in the collapsed overdensity will seek to reach virial equilibrium and form a cosmic object; in the case of under-dense areas, what is left is a void. The outcome of the subsequent nonlinear, gravitational collapse depends on the matter content of the perturbation. The first non-linear objects where formed in dark matter halos with $10^5 - 10^8 M_\odot$ at redshifts between 30 and 10, giving rise to the first stars and massive black holes, which later lead to the formation of galaxy clusters (Mo et al., 2010,Kravtsov and Borgani, 2012). The first objects are the building blocks, in the hierarchical paradigm, of later structure formation though accretion and mergers, which makes a number of physical processes such as cooling, feedback processes and turbulence, relevant to the study of cosmic structure formation, independently of the scale. Galaxy clusters are the most massive objects in the Universe, with masses ranging $10^{13} - 10^{15} M_\odot$. They are characterised by very deep gravitational potential wells containing around 100 to 1000 galaxies over a region of very few Mpc. Although most of the mass in clusters is dark matter, there is a baryonic component of hot and diffuse plasma called the intracluster medium (ICM) permeating the space between galaxies. The ICM, although tenuous (with electron densities $n_e \sim 10^{-4} - 10^{-2}$ cm^{-3}) holds the major part of the baryonic matter in clusters and has temperatures of $T \sim 10^7 - 10^8$ K, causing galaxy clusters to have high X-ray luminosities. It is mainly formed by ionised hydrogen and helium, and a smaller amount of heavier elements.
Apart from observations, N-body simulations have shown that the growth of primordial density perturbations originates a network of cosmic structure interconnected along walls and filaments along a great range of scales (Planelles et al., 2015).

2.2 Missing baryons problem

For decades, cosmologists have been aware that approximately 30% of baryonic matter in the Universe is yet unaccounted for (Shull et al., 2012). This ratio used to be bigger, since the baryon censuses made during the early 90s (Persic and Salucci, 1992) indicated the mass of galaxies was only one-tenth of the baryonic content at high redshift. Baryon abundance can be measured through several methods during the evolution of the Universe: 3 minutes after the Big Bang through primordial nucleosynthesis (through Deuterium abundance), at 300,000 years after the Big Bang by using the angular intensity and polarization fluctuations of the CMB, at redshift $z = 3$ using the Lyman-α clouds, and at lower redshifts using X-ray emission of galaxy clusters. Baryon abundance, however, differs with each of these methods and appears to significantly drop with redshift, as for example, from observations of the Lyman-α forest at $z = 2$ gives a lower limit $\Omega_b \leq 0.035$ (Cen and Ostriker, 1999,Weinberg et al., 1997), while present-day ($z = 0$) measurements provide a lower value from the summed contributions from observed galaxies, X-ray emissions and H_1 and H_2 abundances, $\Omega_b = 0.0068 \pm 0.011$ (2σ limit) (Fukugita et al., 1998).

The theoretical answer to this issue, well-supported by large-scale hydrodynamic cosmological simulations, locates the missing baryons in the Warm-Hot Intergalactic Medium (WHIM) surrounding galaxy clusters in the form of filaments and such LSS, which has temperature ranging between 10^5 <T< 10^7 K at present time (the average temperature of baryons is an increasing function of time). However there is a degree of difficulty detecting them because the largest constituent of the WHIM, hydrogen, is mostly ionised and virtually invisible in ordinary signal-to-noise Far-Ultraviolet (FUV) spectra (Nicastro et al., 2018). Nowadays, it is known that only $\sim 10\%$ of all baryons in the Universe are stellar mass , while $\sim 90\%$ reside in the diffuse and mostly undetected WHIM, either in the circumgalactic medium halos or more diffusely in the intergalactic medium as consequence of feedback processes.

2.3 The CMB and its anisotropies

The CMB, whose discovery in 1965 earned Penzias and Wilson the Nobel prize, is the thermal radiation in the form of a black-body spectrum coming from the surface of last scattering, uniformly observed at $T = 2.728 \pm 0.002$ K, as the COBE mission's instruments detected (Mather et al., 1994) . It was

emitted at redshift $z \simeq 1100$ when baryons and photons decoupled. Prior to decoupling, the Universe was radiation-dominated (there was also a while between matter-radiation equality at $z \sim 3500$ and decoupling when it was matter dominated) and its expansion rate was too high for fluctuations in matter density to gravitationally collapse. Afterwards, when the Universe had already reached $T \sim 3000$ K, photons could travel freely after ions in the cosmic plasma start forming neutral atoms. The CMB radiation that reaches us from that epoch follows Planck's radiation law:

$$I(\lambda, T) = \frac{2hc^2}{\lambda^5} \frac{1}{e^{hc/k\lambda T} - 1}. \tag{2.1}$$

This law is indicative of the dependence of the spectral irradiance I on the wavelength λ and the temperature T of the radiative source.

The CMB, although largely isotropic, shows temperature anisotropies on a scale of the order of $\Delta T/T \simeq 10^{-5}$ K, if we exclude the temperature fluctuations at large scales due to the dipole signal caused by the Solar system's motion in space. Those are caused by primary anisotropies, by which I will be referring to those which were originated during the baryon-photon decoupling, and secondary anisotropies, originated after the surface of last scattering. Primary anisotropies include those caused by gravitational redshift at great scales, acoustic oscillations of the baryon–radiation fluid in the pre-recombination era and damping on small scales. Secondary anisotropies are caused, on one hand, by gravitational effects (photons do not follow straight trajectories when moving through gravitational potentials and General Relativity must be used) such as the gravitational lens effect (Seljak, 1996), the integrated Sachs-Wolfe effect (Sachs and Wolfe, 1967) and the Rees-Sciama effect (Rees and Sciama, 1968), and on the other hand by the interaction between CMB radiation and matter. These effects include the thermal Sunyaev Zel'dovich effect (tSZ) and the kinetic Sunyaev Zel'dovich effect (kSZ), to which next section is dedicated, as well as Thomson scattering due to re-ionization.

2.4 Sunyaev Zel'dovich effect

The Sunyaev–Zeldovich effect (Sunyaev and Zeldovich, 1970) causes a change in the apparent brightness of the cosmic microwave background radiation towards a cluster of galaxies or any other reservoir of hot plasma. The effect takes place through inverse Compton and Thompson scattering in the ionized gas around galaxies and galaxy clusters. The SZ effect consists of two main contributions: the Doppler shifts on the CMB photons due to the bulk flow of the gas, or the kinetic SZ effect, and on the other there's the (Thompson-induced) Doppler shift due to the velocity dispersion of the gas, which is based on the inverse Compton and has briefly been described as the tSZ. What follows is a more detailed overview of both contributions, specially of the kinetic contribution, which is of key importance for this project. The importance of the SZ effect surveys is that they are able to detect all clusters above a certain mass limit independently of the redshifts of the clusters. Recent observations made by the *Planck* mission have found over a thousand galaxy clusters using the SZ effect, including 400 new detections, several superclusters and the first observation of outer-cluster gas bridging two clusters (ESA, 2019).

2.4.1 Thermal Sunyaev-Zel'dovich (tSZ) effect

Hot X-ray emmiting gas (T$\sim 10^8$ K) in galaxy clusters interacts via inverse Compton scattering with the CMB radiation, causing spectral distortions in the CMB radiation in the direction of the cluster. The resulting change in effective temperature of the CMB is given by:

$$\frac{\delta T_{tSZ}}{T_{CMB}} = g(x) \int dl \sigma_T n_e(l) \frac{k_B T_e}{m_e c^2}, \tag{2.2}$$

where $g(x) = x \coth(x/2) - 4$, $x = h\nu/k_B T_{CMB}$ is the nondimensional frequency in terms of the CMB monopole temperature. n_e, T_e, m_e are the electron density, temperature and mass, σ_T is the Thompson cross-section and k_B is the Boltzmann constant. The dependence on frequency of the tSZ-caused temperature shift in the CMB brightness temperature is depicted in Figure 2.1. This effect causes a decrease in the CMB intensity at frequencies $\nu < 218$ GHz and an increase at higher frequencies, allowing

to do observations at various spectral bands around that frequency to determine the cluster position and to determine the tSZ signal characteristics. An example of this can be seen in Figure 2.2 for cluster Abell 2319.

Together with X-ray temperature and luminosity, the $\delta T_{tSZ}/T_{CMB}$ measurements of a cluster may be used to measure its size,gass mass and thermal energy. If the cluster has a low redshift and the curvature effect may be neglected, the angular extent of the tSZ signal of the cluster yields a measure of the Hubble constant (Mo et al., 2010).

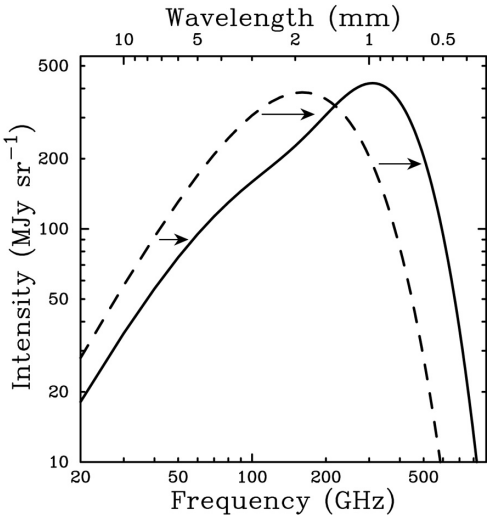

Figure 2.1: From Carlstrom et al., 2002, CMB spectrum undistorted (dashed line) and distorted by the Sunyaev-Zel'dovich effect (solid line). SZ effect distortion shown is for a fictional cluster 1000 times more massive than a typical massive galaxy cluster. The SZ effect causes a decrease in the CMB intensity at frequencies $\nu < 218$ GHz and an increase at higher frequencies.

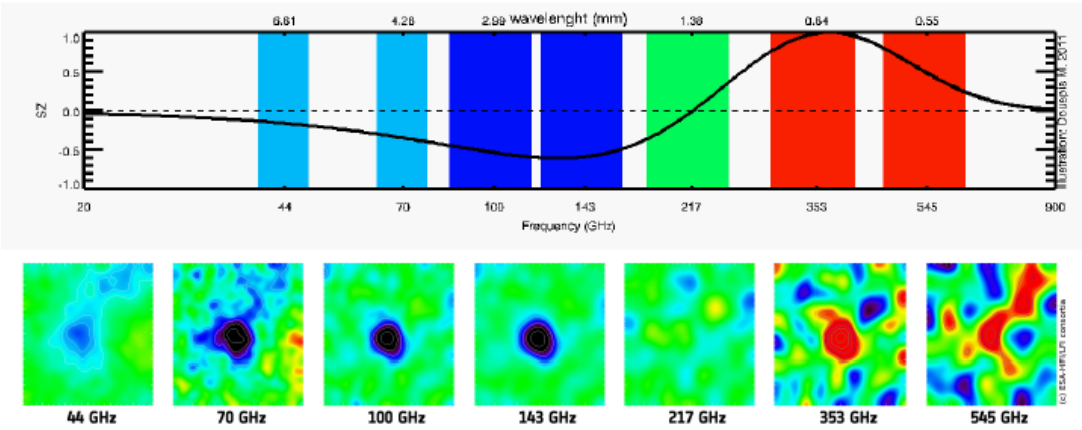

Figure 2.2: From Douspis, 2011, galaxy cluster Abell 2319 seen by Planck telescope in various band frequencies (shown in top panel) between 44 GHz and 545 GHz. The signature tSZ dependence on frequency is patent in the bottom panel image.

2.4.2 Kinetic Sunyaev-Zel'dovich (kSZ) effect

The kinetic component of the SZE describes the Doppler boost the CMB photons experience through Thompson scattering when interacting with a moving cloud of ionised gas, regardless of it being free or bound to structures such as galaxy clusters or groups. It depends on the integral of the number density of free electrons and their relative velocity with respect to the CMB frame (peculiar velocity) in the LOS direction. The equation describing it is written as follows

$$\frac{\delta T_{kSZ}(\hat{\boldsymbol{n}})}{T_{CMB}} = -\int_0^{x_{\rm LSS}} \frac{dx}{1+z} n_e(\hat{\boldsymbol{n}}, z)\sigma_T e^{-\tau(z)} \frac{\boldsymbol{v}_e \cdot \hat{\boldsymbol{n}}}{c}, \tag{2.3}$$

where x is the comoving distance at redshift z, σ_T is the Thompson cross-section, $\tau(z)$ stands for the optical depth to Thompson scattering at a redshift z along the line of sight and $\hat{\boldsymbol{n}}$ is a unitary vector giving the direction of observation. The integral formally extends to the distance to the surface of last scattering ($x_{\rm LSS}$). The optical depth can be expressed as

$$\tau(z) = \int_0^{x(z)} \frac{dx'}{1+z'} n_e(x', \hat{\boldsymbol{n}})\sigma_T,$$

where n_e is the physical (not comoving) electron number density. After recombination at $z = 1100$ the electron density dropped dramatically, and then increased again during the reionization epoch at $z \sim 7{-}9$. Because of this, the measured value of the optical depth lies at the level of $\tau \sim 0.05$. This is the sky average value of τ, but when looking along a line of sight towards a galaxy cluster it may be significantly different. However, it is valid to assume $\exp\tau(z) \approx 1$ for low redshifts ($z < 5$). Due to the increase of physical electron number density in clusters with redshift, both tSZ and kSZ have higher amplitudes at higher redshift. Additionally, because of the different mass scaling of electron temperature ($T_e \propto M^{2/3}$) with respecdt to that of the radial peculiar velocity (which is largely independent of the mass), we expect a bigger ratio of kSZ over tSZ for decreasing masses. According to Hernández-Monteagudo et al., 2006, at $z = 0$ we see clusters with masses below 10^{15} $M_\odot$ should produce more kSZ than tSZ flux at 222 Ghz, at least by a factor of a few.

In the last decade, work has been done regarding the link between kSZ and the detection of the missing baryons. An example of such is the collaboration by Hernández-Monteagudo et al., 2015. In it, *Planck* measurements and the Central Galaxy (CGs) catalogue provided by the Sloan galaxy survey are used to probe regions around CGs using the kSZ pairwise peculiar momentum and the cross correlation function of the kSZ temperature and the recovered radial peculiar velocity. They conclude that the probed regions contain roughly half the total amount of baryons in the Universe at that epoch.

3. Semi-analytical methodology

El procedimiento semi-analítico llevado a cabo parte de la Ec.(2.3) para hacer una estimación del kSZ procedente de halos de distintas masas comprendidas entre 10^{13}-10^{15} $h^{-1}M_{\odot}$. Para ello, se digitalizan los perfiles de sobredensidad bariónica para distintos intervalos de masas de halos del artículo de Chaves-Montero et al., 2021, que fueron obtenidos mediante simulaciones usando el Borg Cube (Emberson et al., 2019). Los perfiles de sobredensidad iniciales (a un halo, con distintos intervalos de masa) se extrapolan y modifican teniendo en cuenta la distribución espacial de halos que pueden contribuir a la señal de kSZ por encontrarse muy cerca de la línea de visión, también llamada contribución a dos halos. El término a dos halos se obtuvo siguiendo el modelo de la función de masa que expone el artículo de Ondaro-Mallea et al., 2022. Además, se lleva a cabo un desarrollo teórico a través de teoría lineal de perturbaciones que culmina en la estimación de la correlación espacial de las velocidades radiales peculiares, la cual depende de la masa de los halos y de su redshift, así como la escala que se decide utilizar para el suavizado por medio de la función ventana. Los resultados obtenidos del flujo de kSZ proveniente del interior de los halos tienen una magnitud coherente con lo que se esperaba en teoría, y también tienen la dependencia lineal esperada con la masa de los halos. La comparación del flujo de kSZ proveniente de los halos con el flujo proveniente de cilindros a lo largo de la línea de visón de distintas profundidades centrados en los halos dejan ver que la contribución del medio ionizado fuera de los halos oscila entre el $10 - 35\%$ del total. Este porcentaje de contribución a la señal kSZ de los electrones libres viene condicionada por la masa de los cúmulos de galaxias, siendo mayor para cúmulos de bajas masas y en los casos en los que se observa el flujo de un cilindro de mayor profundidad en la línea de visión. En este caso, la suma de sobredensidades (contribuciones a un halo y a dos halos) modulada por la correlación de la velocidad peculiar de los electrones lleva asociada una menor contribución relativa del medio intracumular a la señal de kSZ, ya que predomina la contribución propia del halo. Los resultados del modelo analítico dependen, por otra parte, de la escala de suavizado usada para el campo de velocidades, ya que cuanto menor es esta escala, menor es el número de electrones externos al halo que consideramos que producen efecto kSZ.

The aim of this chapter is to explain the semi-analytical approach to the calculation of the halo contribution to the kSZ temperature distortion along a line of sight (LOS), the results of which will be analysed in the next chapter. This chapter will therefore be focused on examining cosmic density and velocity fields in the context of Newtonian perturbation theory in the linear regime. As was seen in the explanation of the kSZ given in §*2.4*, the modelling of these two is crucial to make a valid model of the kSZ signal coming from a certain parcel of IGM located at some point in the Universe. To do so, this chapter begins by describing in §*3.1* the growth of cosmological perturbations in the linear regime and their statistical properties as a Gaussian perturbation field in §*3.2*, including the linear power spectrum. The theory covering the topic of large scale mass distribution is summarised in §*3.3*, where I also specify the one-halo overdensity term used for this project. The two-halo term is introduced in §*3.4* to modify the original overdensity data and take into account the kSZ contribution of other galaxy clusters which are nearby the LOS of the observed cluster. The large scale velocity field needed to modulate the amount of electrons contribution to the kSZ is modelled in §*3.5*. The results obtained using the semi-analytic model are finally included in §*3.6*.

3.1 Newtonian Theory of Small Perturbations for an ideal fluid

The Universe is assumed to have been homogeneous at early times, with LSS growing from small initial density perturbations due to the action of gravity. The evolution of those perturbations is in the linear regime when the density contrast relative to the background is much smaller than unity; it is therefore applicable to structures with sizes smaller than the horizon size. The growth of the inhomogeneities later entered a non-linear evolution phase during which small and then large scale structure began to form. Newtonian small order perturbation theory can be used to study the evolution of a non-relativistic fluid of density ρ and velocity $\mathbf{u}$ under the influence of a gravitational field with potential Φ. This may be done in the framework of FLRW metric and is well-suited to study the early Universe, when the density contrast in fluctuations was less than unity. The fluid description is valid for baryonic gas and for collisionless dark matter, more abundant than the former; the equations that describe its evolution are (Mo et al., 2010, page 163):

$$\text{Continuity}: \quad \frac{D\rho}{Dt} + \rho \nabla_{\boldsymbol{r}} \boldsymbol{u} = 0 \tag{3.1}$$

$$\text{Euler}: \quad \frac{D\boldsymbol{u}}{Dt} = \frac{-\nabla_{\boldsymbol{r}} P}{\rho} - \nabla_{\boldsymbol{r}} \Phi \tag{3.2}$$

$$\text{Poisson}: \quad \nabla^2_{\boldsymbol{r}} \Phi = 4\pi G \rho \tag{3.3}$$

where $\boldsymbol{r}$ is the proper coordinate and D/Dt is the material derivative. In an expanding FLRW Universe, it is useful to employ comoving coordinates $\boldsymbol{x}$, defined as

$$\boldsymbol{r} = a(t)\boldsymbol{x} \tag{3.4}$$

The proper velocity $\boldsymbol{u} = \partial \boldsymbol{r}/\partial t$ can be written as a function of peculiar velocity (seen by a comoving observer) $\boldsymbol{v} = \boldsymbol{x} \cdot \partial a(t)/\partial t$:

$$\boldsymbol{u} = \frac{\partial a(t)}{\partial t}\boldsymbol{x} + \boldsymbol{v}. \tag{3.5}$$

Replacing the proper coordinate system with the comoving, i.e $(\boldsymbol{r}, t) \to (\boldsymbol{x}, t)$, changes the derivatives as well, making $\nabla_{\boldsymbol{r}} \to \nabla_{\boldsymbol{x}}/a$, $\partial/\partial t \to \partial/\partial t - \dot{a}\boldsymbol{x} \cdot \nabla_{\boldsymbol{x}}/a$. We introduce the density contrast, which is defined as

$$\delta(\boldsymbol{x}, t) = \frac{\rho(\boldsymbol{x}, t)}{\overline{\rho}(t)} - 1, \tag{3.6}$$

with the mean density $\overline{\rho}(t) \propto a^{-3}$. Introducing ρ in terms of δ into the previous equations and writing them in comoving coordinates:

$$\frac{\partial \delta}{\partial t} + \nabla[(1+\delta)\boldsymbol{v}] = 0 \tag{3.7}$$

$$\frac{\partial \boldsymbol{v}}{\partial t} + \frac{\dot{a}}{a}\boldsymbol{v} = \frac{-\nabla \Phi}{a} - \frac{\nabla P}{a\overline{\rho}(1+\delta)} \tag{3.8}$$

$$\nabla^2 \Phi = 4\pi G \overline{\rho} a^2 \delta. \tag{3.9}$$

For the case of a pressureless fluid, such as dark matter, the differentiation with respect to time results in

$$\frac{\partial^2 \delta}{\partial t^2} + 2\frac{\dot{a}}{a}\frac{\partial \delta}{\partial t} = 4\pi G \overline{\rho} \delta, \tag{3.10}$$

which in Fourier space is

$$\frac{d^2 \delta_{\boldsymbol{k}}}{dt^2} + 2\frac{\dot{a}}{a}\frac{d\delta_{\boldsymbol{k}}}{dt} = 4\pi G \overline{\rho} \delta_{\boldsymbol{k}}. \tag{3.11}$$

From Mo et al., 2010 page 172, we know that the Hubble term follows the equation

$$\frac{d^2 H}{dt^2} + 2\frac{\dot{a}}{a}\frac{dH}{dt} = 4\pi G \overline{\rho} H \tag{3.12}$$

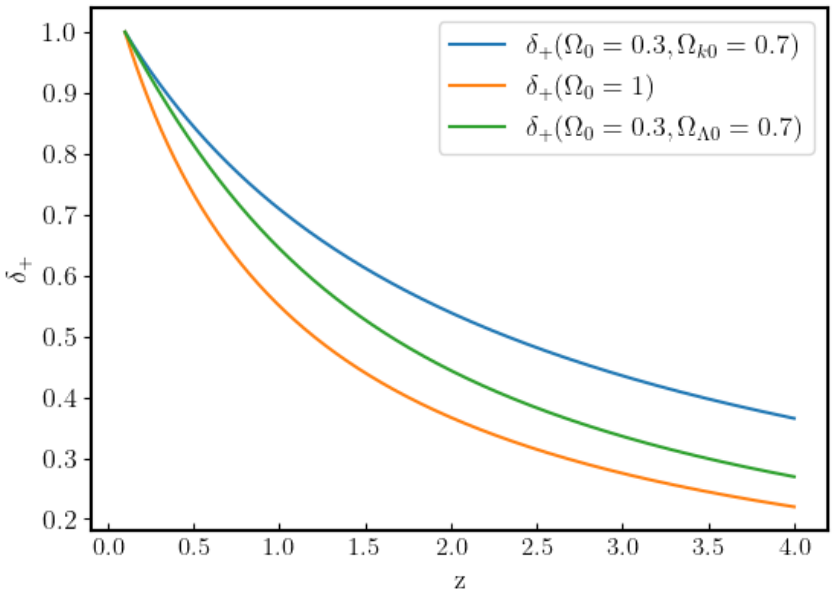

Figure 3.1: Growing mode δ_+ for fluctuations in different cosmological models calculated using Eq.3.13, the most relevant being the one in accordance with the ΛCDM model ($\Omega_\Lambda = 0.7$ and $\Omega_0 = 0.3$). In this case, the growth of fluctuations starts happening at $z > 1$.

so because $\delta_{\boldsymbol{k}}$ and H(t) obey the same equation, the decreasing mode will be $\delta_- \propto H(t)$ and the growing mode is

$$\delta_+ \propto H(t) \int_0^t \frac{dt'}{a^2(t')H^2(t')} \propto a_0^2 H_0^2 E(z) \int_z^\infty \frac{dz'(1+z')}{E^3(z')} \tag{3.13}$$

where $a_0 = 1$, the Hubble parameter used is $H_0 = 100$ km/s/Mpc and the $E(z)$ function is

$$E(z) = \left[(\Omega_0 z + 1)(1+z)^2 - \Omega_{\Lambda,0} z(2+z)\right]^{1/2} \tag{3.14}$$

Also, we have that $\delta_+ \propto D_\delta(z)$ with $D_\delta(z)$ the linear growth rate. The growing mode can be obtained from numerically from Eq.(3.13). Figure 3.1 shows the growing mode for different cosmological models. For models with high matter density ($\Omega_0 \to 1$), the growth of structure from fluctuations is seen to happen more close to $z = 0$ than those with a non-zero dark energy component or open universes, where the growth happens at $z > 1$. In them, expansion rate is larger than in an Einstein de Sitter universe and the perturbation growth is reduced because of the enhanced Hubble drag. In the following we use the one that follows the concordance model, with $\Omega_\Lambda = 0.7$ and $\Omega_0 = 0.3$.

3.2 Statistical properties of a Gaussian random field

In order to determine a cosmic density field, which is considered to be the realisation of a random process, it is useful to know its statistical properties. Dividing the Universe into a n infinitesimal cells centred at $\mathbf{x}_1$, $\mathbf{x}_2$ ... $\mathbf{x}_n$, the probability distribution function that characterises the random perturbation field $\delta(\mathbf{x})$ is

$$P_x(\delta_1, \delta_2, ..., \delta_n) d\delta_1 d\delta_2 ... d\delta_n$$

and it indicates the probability of the δ field having values in the range δ_i to $\delta_i + d\delta_i$ at positions $x_i (i = 1, 2, ..., n)$ (Mo et al., 2010). The cosmological principle states that the Universe is homogeneous and isotropic, so there is spatial invariance under translation and rotation. The mean of the density perturbation field is therefore null, and its two-point correlation function only depends on distance, such that

$$\xi(\boldsymbol{x}_1 - \boldsymbol{x}_2) = \xi(|\boldsymbol{x}_1 - \boldsymbol{x}_2|) = \langle \delta(\boldsymbol{x}_1) \delta(\boldsymbol{x}_2) \rangle. \tag{3.15}$$

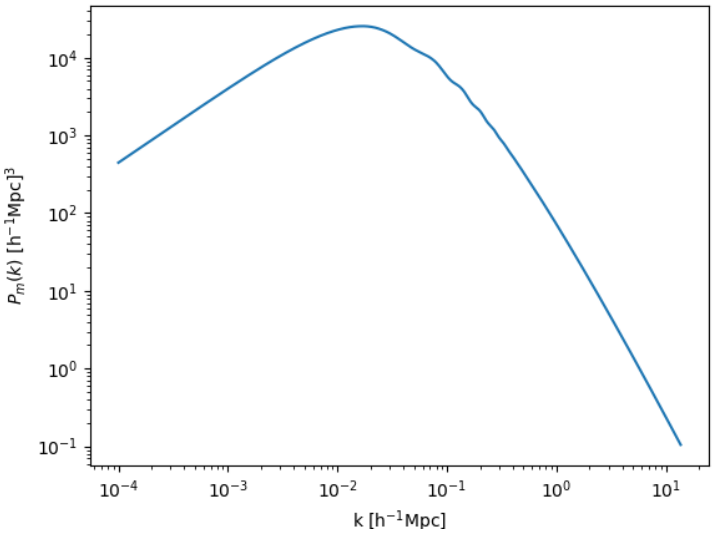

Figure 3.2: CAMB matter power spectrum for the ΛCDM model.

Also, $\xi(0) = \sigma^2$ where σ^2 is the variance of the perturbation field. Representing the density perturbation field by its Fourier mode

$$\delta_{\boldsymbol{k}} = \frac{1}{V_u} \int \delta(\boldsymbol{x}) \exp\left(-i\boldsymbol{k} \cdot \boldsymbol{x}\right) d^3\boldsymbol{x}. \tag{3.16}$$

The power spectrum is then defined as

$$P(k) = \int \xi(\boldsymbol{x}) \exp\left(-i\boldsymbol{k} \cdot \boldsymbol{x}\right) d^3\boldsymbol{x}. \tag{3.17}$$

Conversely, the two-point correlation function can be expressed as

$$\xi(x) = \frac{1}{(2\pi)^3} \int P(k) \exp\left(i\boldsymbol{k} \cdot \boldsymbol{x}\right) d^3\boldsymbol{k}, \tag{3.18}$$

so the two-point correlation function is the Fourier transform of the power spectrum. A Gaussian field is a random field such that the distribution of field values at an arbitrary set of n points is an n-variate Gaussian. It is applicable to the initial density field because Gaussian perturbations are given rise by quantum fluctuations in the inflationary period; this has been verified by observational evidence. Also, a Gaussian field has the property of remaining Gaussian during linear evolution.

The initial density power spectrum for a ΛCDM model, with $\Omega_{\Lambda 0} = 0.7$ and $\Omega_{m0} = 0.3$, has been obtained through the Code for Anisotropies in the Microwave Background, CAMB (Lewis and Challinor, 2011) [1] to reproduce observational measurements of the CMB anisotropies. In Figure 3.2 it is represented between k values 10^{-4}-0.1 h/Mpc, although here, integrations involving the power spectrum will usually be made between values 10^{-3}-1 h/Mpc, which belong to the linear regime. Higher k corresponds to smaller scales, in which linearity is no longer applicable.

3.3 Large-scale mass distribution

The statistical characterisation of the cosmic density field consists of the statistics of density and velocity fields of matter in the Universe. The two-point correlation function of the density field has already been defined, as has also been mentioned that it forms a Fourier transform pair with the power spectrum.

At this point, a top-hat, spherically symmetric, window smoothing function W(x) is introduced such

[1] https://camb.readthedocs.io/en/latest/index.html

that

$$W(\boldsymbol{x};R) = \left(\frac{4\pi}{3}R^3\right)^{-1} \begin{cases} 1 & \text{if } |\boldsymbol{x}| < R \\ 0 & \text{if } |\boldsymbol{x}| \geq R \end{cases}$$

where R is the radius of the spherical function and x the comoving coordinate. The Fourier transform of the top-hat window function is

$$W_{\boldsymbol{k}}(R) = \frac{3}{(kR)^2}\left(\frac{\sin(kR)}{kR} - \cos(kR)\right). \tag{3.19}$$

The measured density has the property of being an averaged estimate throughout the volume given by $W(x;R)$, which constitutes a convolution, and which, in Fourier space, can be written as a product of δ_k with $W_k(R)$, hence

$$\delta(\boldsymbol{x};R) = \int \delta(\boldsymbol{x'})W(\boldsymbol{x}-\boldsymbol{x'};R)d^3\boldsymbol{x'} \;;\; \delta_{\boldsymbol{k}}(R) = \delta_{\boldsymbol{k}}W_{\boldsymbol{k}}(R). \tag{3.20}$$

A radius R big enough smooth over the smaller non-linear scales should be used for the above equation. The scales at which perturbation modes start to couple due to non-linear gravitational evolution plus other astrophysical processes and reach the non-linear regime are those below 30-50 h^{-1} h^{-1}Mpc. Calculating the variance of the number counts within randomly placed spheres of given radius r, one finds that at $r \approx 8\ h^{-1}$Mpc the rms of the (smoothed) density contrast field approaches unity. Integrating in the angle between **k** and **x** from Eq.(3.18) and including $W_{\boldsymbol{k}}(R)$, the two-point correlation function results in the expression

$$\xi(x,R) = \frac{1}{2\pi^2}\int_{k_{min}}^{k_{max}} k^3 P(k) J_0(kx) |W_{\boldsymbol{k}}(R)|^2 \frac{dk}{k} \tag{3.21}$$

where $J_0(kx)$ is the zero order Bessel function and, typically, the chosen values for the k integration limits are $k_{min} = 10^{-3}$ and $k_{max} = 1\ h$/Mpc, as they are considered to be limit values for the linear regime. Because the window function decreases faster with k than $J_0(kx)$, the measure of the power spectrum is made smoother at $k = 2\pi/x$. Also, the main contribution to the integral $\xi(x,R)$ comes from $k \leq 1/x$, where the window function is close to unity.

3.3.1 Gas overdensity profiles

In order to obtain the kSZ contribution from a galaxy cluster compared to the total kSZ signal along a LOS in the direction of the cluster, it is necessary to have a model of the baryonic mass distribution around the cluster center. The baryonic gas overdensity profiles of clusters in a distance range $0.1 - 10$ h^{-1}Mpc have been obtained from Chaves-Montero et al., 2021, hereafter referred to as CM21, where a Borg Cube cosmological hydrodynamical simulation has been used to get four profiles for four different cluster mass bins at $z = 0.24$. Cluster masses used here range between $10^{13} - 10^{15}\mathrm{M}_\odot/h$, and the mass bins are equally spaced in the log scale. The Borg Cube simulation only incorporates non-radiative baryonic processes and the results hold up to redshift $z = 4$. Figure 3.3 has been digitised from CM21 in order to use its results for this project. It shows the overdensity profiles for the four mass bins and the three comparative fits used in the article: double exponential and β-profiles, both of which are rather good fits for the data, and Gaussian profiles, which are not and are therefore ignored. The β-profiles follow the equation $\Delta_{gas}(r) = \Delta_b[1 + r^2/r_s^2]^{-3/2} + 1$, while the double exponential profiles follow $\log \Delta_{gas}^{exp}(r) = \Delta_b' \exp\left[-(r/r_s)^{3/4}\right]$ [2]. Both these formulas have been used to extend the overdensity profiles to further distances from the halo center, as well as closer to it. The extension in shown in Figure 3.4, where the profile has been obtained in a range from 1 h^{-1}kpc to 200 h^{-1}Mpc (the explanation of how this profile must again be modified to account for the gas contribution from other clusters close to the LOS will be given later). The way it was extrapolated was by making use of the β profile equation when $r < 0.11\ h^{-1}$Mpc, and the double exponential when approaching $\Delta_{gas}(r) \sim 1$, making $\Delta_{gas}(r) = 1$ if the fit gave $\Delta_{gas}(r) < 1$. This is an approximation made manually by me which may be biased, specially toward the extension made close to center of the halo, due to the lack of data at these distances. I will

[2] The two equations for the β and double exponential fit do not follow the same expressions used in CM21, as those apparently included typos.

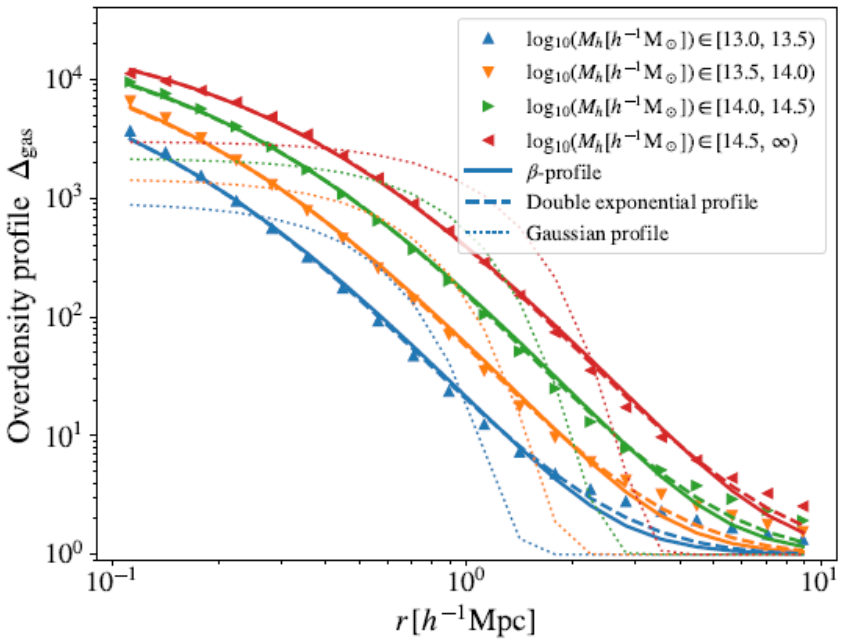

Figure 3.3: As extracted from CM21: Large-scale distribution of gas surrounding haloes of different masses as predicted by the cosmological hydrodynamical simulation Borg Cube. Symbols indicate results from the simulation at $z = 0.24$, while solid, dashed, and dotted lines denote the best-fitting solution to these using β, double exponential, and Gaussian profiles, respectively. We can readily see that the β and double exponential profiles capture simulation results precisely, while Gaussian profiles provide a lousy fit to data.

also neglect the redshift dependence of this fit with moderate impact, since it involves a relatively small range of distances in a usually wider radial integral. This is assumed to be a good enough approximation for this project and thus I proceed to use it as an estimation of the density field needed to calculate the kSZ via Eq.(2.3).

3.4 Mass function of dark-matter halos

At first sight, the density profiles from CM21 would seem sufficient to explore the kSZ coming from the halos compared to the kSZ including bound electrons only (at $r < R_{200}$). Initially, this was the plan for this project, however, we were not getting the expected results just using these distributions. I then realised that were not taking into account the contribution due to other clusters in the same or close enough to the LOS to be contributing to the kSZ signal as well. It so happens that it is possible that while observing a certain cluster, there may be clusters positioned in such a way that the moving plasma in and around them is contributing to the kSZ of the observed cluster. This situation is depicted in Figure 3.5, where the contaminating cluster is positioned before the observed one, but it would be contaminating as well if it were behind it. This means the overdensity will have a second contribution given by the halo mass distribution along the LOS, so now

$$\Delta_g(\boldsymbol{r}) = \Delta_g^{1h}(\boldsymbol{r}) + \Delta_g^{2h}(\boldsymbol{r}) \tag{3.22}$$

where the two-halo contribution is expressed as

$$\Delta_g^{2h}(\boldsymbol{r}|\boldsymbol{r}_1 M_1) = \int d\boldsymbol{y} dM \frac{dn}{dM}(y) \Delta_g^{1h}(|\boldsymbol{y} - \boldsymbol{r}|) \tag{3.23}$$

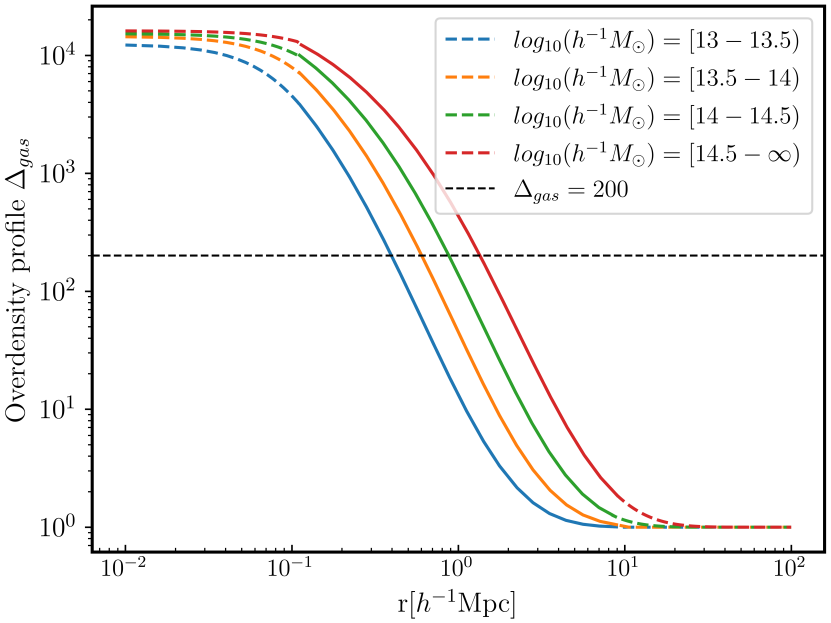

Figure 3.4: Extended gas overdensity profiles. Solid lines represent the part of the fit directly obtained from CM21, dashed coloured lines represent the extrapolated data using the β and double exponential fits. Dashed black line represents the overdensity at which clusters reach their virial radii R_{200}.

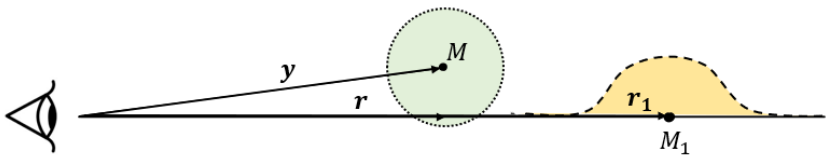

Figure 3.5: Schematic view of a cluster with mass M and position vector $\boldsymbol{y}$ having some of its ionised gas in the LOS of the observed cluster of mass M_1 and position vector $\boldsymbol{r}_1$.

where dn/dM is the halo number density with respect to mass and $\Delta_g^{1h}(\boldsymbol{r})$ is the halo contribution already calculated with the data from CM21. The halo number density is calculated as

$$\frac{dn}{dM}(y|M_1, r_1) = \frac{d\bar{n}}{dM}(1 + b(M_1, z_1)b(M, z_1))\xi_m(y) \tag{3.24}$$

or similarly,

$$\frac{dn}{dM}(\boldsymbol{y}) = \frac{d\bar{n}}{dM}(1 + \xi_{h_1h_2}(\boldsymbol{r_1} - \boldsymbol{y})), \tag{3.25}$$

with $\xi_m(y)$ being the matter correlation function. Plugging this into Eq.3.23 gives

$$\Delta_g^{2h}(\boldsymbol{r}|\boldsymbol{r}_1 M_1) = \int d\boldsymbol{y} dM \frac{d\bar{n}}{dM}(1 + \xi_{h_1h_2}(\boldsymbol{r}_1 - \boldsymbol{y}))\Delta_g^{1h}(|\boldsymbol{y} - \boldsymbol{r}|), \tag{3.26}$$

with the halo correlation function being

$$\xi_{h_1h_2}(\boldsymbol{x}) = b_1(M_1, z_1)b_2(M_2, z_2) \int \frac{d\boldsymbol{k}}{(2\pi)^3} e^{-i\boldsymbol{k}\cdot\boldsymbol{x}} P_m(\boldsymbol{k}) W_k(R[M_1]) W_k(R[M_2]). \tag{3.27}$$

This term has already been calculated except for the bias factors $b_1(M_1, z_1)$ and $b_2(M_2, z_2)$, which account for the halos'extra or biased clustering. Equations 3.26 and 3.27 are solved with the model taken from the article by Ondaro-Mallea et al., 2022, hereafter mentioned as OM22. In accordance with the Press-Schechter formalism (Press and Schechter, 1974), the expression for the number of dark matter halos of mass M is given by the relative abundance of peaks in a Gaussian random field, such that

$$n(M) d\log M = \frac{-1}{3} \frac{\rho_b}{M} \frac{d\log\sigma}{d\log M} \nu f(\nu), \tag{3.28}$$

where ρ_b is the background matter density of the universe; $f(\nu) = \sqrt{2/\pi}\exp(-\nu^2/2)$; ν is the peak height associated to a halo of mass M, $\nu = \delta_c/\sigma(M, z)$; $\delta_c = 1.868$ is the critical overdensity for collapse and $\sigma(M, z)$ is the rms linear variance at redshift z. On the other hand, σ is the matter linear rms at redshift z within a sphere of radius equal to the Lagrangian radius of a halo of mass M. Such radius is defined as

$$R = \left(\frac{3M}{4\pi\bar{\rho}_m}\right)^{1/3}. \tag{3.29}$$

The linear variance is expressed as a function of this radius and of the redshift, such that

$$\sigma(R, z) = \frac{D_\delta^2(z)}{2\pi} \int_0^\infty P_m(k)|W_k(R)|^2, \tag{3.30}$$

where $D_\delta(z)$ is the linear growth factor. The article OM22, proves that the halo mass function generically depends on growth rate and and power spectrum shape . To do it, they characterise each halo by an "effective growth rate" (α_{eff}) and an effective "local power spectrum slope" (n_{eff}) aimed at capturing how fast halos have lately grown and the density profile of the collapsing region. They are respectively defined as

$$\alpha_{eff}(a) = \frac{d\log(D)}{d\log a}|_{a=a_{ev}} \; ; \; n_{eff}(a) = -3 - 2\frac{d\log\sigma(R)}{d\log R}|_{\kappa R_L(M)}, \tag{3.31}$$

where $a = (1 + z)^{-1}$ is the expansion factor. They use the factor $D(a_{ev}) = \gamma D(a)$ with $\gamma = 4/5$ to take into account the recently accreted amount of mass. For the power spectrum slope, $\kappa = 1$ and $R_L(M)$ is the Lagrangian radius. The way in which this particular work models the dependence of the halo mass function with the growth rate and slope of the power spectrum is via a functional of the form $\nu f(\nu) = \nu f_1(\nu) f_2(n_{eff}) f_3(\alpha_{eff})$. The functional form is described in detail in Equations (5)-(8) of OM22. In Table 3 of this article we find the best-fitting parameters, which have also been used for this project (see fourth row of Table 3 in OM22).

As for the bias of dark matter halos, its square is the ratio of the halo power spectrum to the linear dark matter power spectrum. In Tinker et al., 2010 a bias fitting function is derived and it corresponds to Eq.(6) of said article, which also provides the best-fit values for this parametrisation. These have been

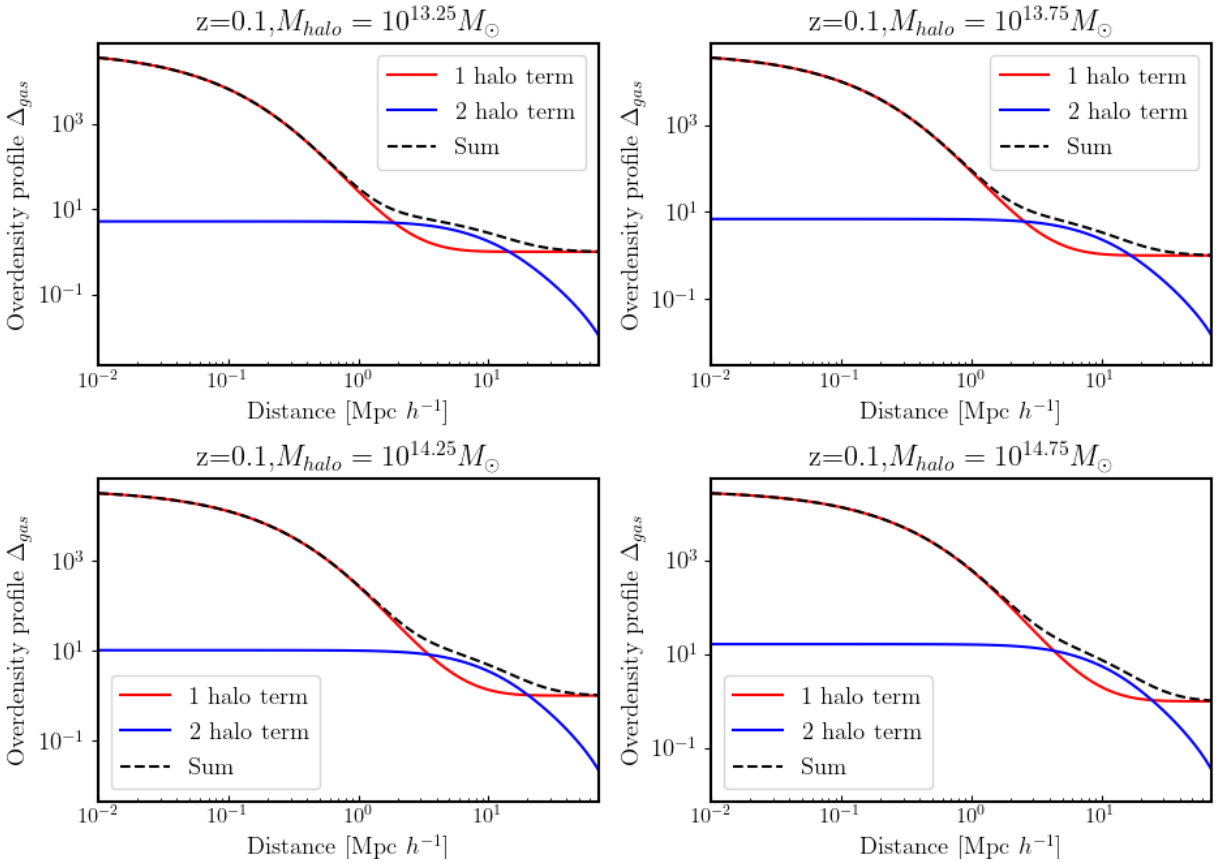

Figure 3.6: Overdensity profiles for four halo masses, which are the central values for the halo mass bins used in CM21, and for redshift $z = 0.1$. The blue solid lines represent the two-halo contribution, the solid red lines represent the one-halo contribution and the dashed black line is the sum of the two as a function of distance from the center of the cluster.

used by my supervisor, Dr.Carlos Hernández-Monteagudo, to obtain a code which parameterises and obtains the two-halo correlation term, which summed to the previously exposed one-halo term, gives a good description of the gas overdensity surrounding a galaxy cluster. It is worth mentioning that the new overdensity profiles will have an explicit dependence on redshift through the two-halo term. This can be seen in the Figure B.1, where, for four mass examples, the summed terms are shown for different redshifts ($z = 0.5, 1.0, 1.5$). Clearly, the two-halo contribution decreases at higher redshifts, and more massive halos have a higher two-halo contribution. Figure 3.6 shows the one-halo and two-halo contribution for four mass examples, which are the middle logarithmic values of the mass bins used in CM21, for redshift $z = 0.1$. In this figure we see how for bigger masses the two-halo contribution reaches a greater extension and has a bigger amplitude, dropping to the overdensity unity plateau at higher distances from the halo center. This gives an idea that higher mass halos will have more kSZ inducing electrons along the LOS than lower mass halos but still, this will be modulated by the velocity correlation between them, which is discussed in the following sections.

3.5 Large-scale velocity field

Measurements of the linear velocity field are very valuable because they provide direct constraints on the mass density field. This is due to the peculiar velocities induced by density perturbations in the linear regime ($\delta \ll 1$) being proportional to the amplitude of the density fluctuations,

$$\boldsymbol{v_k} = \frac{ia\boldsymbol{k}}{k^2}\frac{d\delta_{\boldsymbol{k}}}{dt}. \tag{3.32}$$

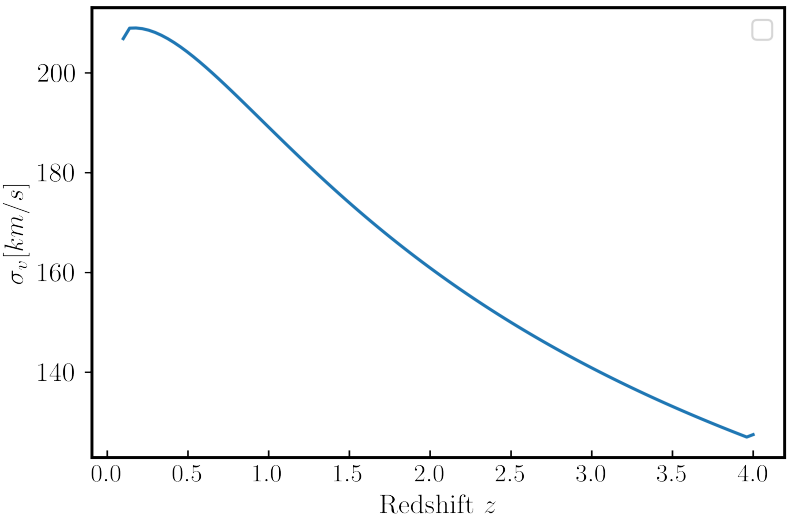

Figure 3.7: Velocity field rms $\sigma_v(z)$ as a function of redshift, calculated using smoothing scale R=15 Mpc/h.

At the time when the growing mode $\delta_+ \propto D_\delta(z)$ is dominant, we find that, after plugging in Eq.(3.13),

$$\boldsymbol{v_k} = \frac{i\boldsymbol{k}}{k^2} H(z)\delta_{\boldsymbol{k}} \frac{dD_\delta}{dz}. \tag{3.33}$$

Therefore, the variance of the *radial component* of the velocity field is expressed as

$$\sigma_v^2(R,z) = \frac{1}{3}\left|H(z)\frac{dD_\delta}{dz}\right|^2 \int_{k_{\min}}^{k_{\max}} \frac{dk}{2\pi^2} P_m(k)|\mathrm{W}_{\boldsymbol{k}}(R)|^2, \tag{3.34}$$

where again, it is seen that the velocity variance is sensitive to the Lagrangian scale R associated to a cluster mass M. Galaxy clusters are supposed to be better tracers of the linear velocity field than galaxies, as they represent the largest virialised structures in the Universe. The peculiar velocity of a cluster probed by the kSZ effect, can be interpreted as the linear peculiar velocity field smoothed on a comoving scale where the linear regime still applies. For the sake of simplicity, we shall assume a fixed Lagrangian scale equal to 30 h^{-1} Mpc, although we also tried 15 h^{-1} Mpc, or a mass-dependent Lagrangian scale given by Eq.3.29. We ended up adopting 30 h^{-1} Mpc since this should correspond to a 'safe' linear scale at recent epochs. In Fig.3.7 the velocity field rms is shown manifesting its dependence with redshift and we can see that the values of the velocity amplitudes decrease with redshift. This description of the velocity field is yet incomplete as knowing the amplitude of the velocity field is not enough, we must also know the velocity correlation of the cluster gas as a function of distance from the cluster's center.

3.5.1 Peculiar velocity field approximation

In order to model the correlation of the peculiar velocity field around the galaxy cluster center, an approximation was made such that

$$\langle|\mathbf{v}(x,R,z)\cdot\hat{\mathbf{n}}|\rangle = v_i(x,R,z) \simeq f(x)\sigma_v(R,z), \tag{3.35}$$

where the cluster mass M may trivially replace R (see Eq.(3.29)) as an independent parameter on which the peculiar velocity depends. The function $f(x)$ represents the normalised velocity correlation function, dependent on the distance x along the LOS from the cluster center to any point along the LOS. It was modelled under the assumption that the velocity field is Gaussian and isotropic. It is necessary to

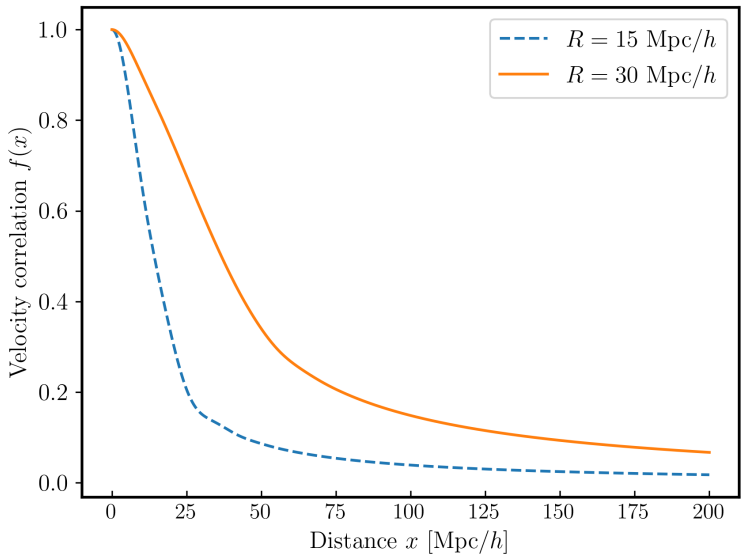

Figure 3.8: Normalised peculiar velocity correlation function $f(x)$ using smoothing functions over $R = 30$ Mpc/h (solid line) and $R = 15$ Mpc/h (dashed line).

integrate in two dimensions and in k to obtain the LOS component:

$$f(x_1 - x_2) = \frac{\langle v_1 \cdot v_2 \rangle (x_1 - x_2)}{\langle v^2 \rangle_{x=x_1}} = \frac{\langle v_1 \cdot v_2 \rangle (x_1 - x_2)}{\sigma_v^2} = \frac{\int\int\int d\phi d\mu dk \frac{k^2}{2\pi^2} \exp(-ikr\mu) \frac{P_m(k,z)}{k^2} |W(k,R)|^2}{\int\int\int d\phi d\mu dk \frac{k^2}{2\pi^2} \frac{P_m(k,z)}{k^2} |W_R(k)|^2},$$

where $\mu = \cos\theta$ and $P_m(k,z) \propto P_m(k) D^2(z)$. We define $x_2 = 0$ as the initial cluster's center and $x = x_1$. After solving the integrals, most terms cancel out leaving the expression

$$f(x) = \frac{\int P_m(k) |W_R(k)|^2 J_0(kx) dk}{\int P_m(k) |W_R(k)|^2 dk}, \tag{3.36}$$

where $J_0(kx)$ is the zero-Bessel function that gives the dependence of the velocity correlation with distance from the cluster center.
The radius for the window function was chosen following the criteria that at 30 h^{-1}Mpc linear theory is valid and that linearity starts to break down at scales smaller than the Lagrangian radius of the cluster, which is 14.2 Mpc in the case of 10^{15} $h^{-1} M_\odot$. The result from Eq.(3.36) is portrayed in Figure 3.8, where it is apparent that the electron velocity is still correlated at a distance of a few Mpc and starts to slowly drop off, approaching null correlation beyond 200 Mpc h^{-1}. It will be further discussed whether it is possible to apply a smoothing scale of (a somewhat arbitrary) 15 Mpc instead of 30 Mpc h^{-1}, and the change induced in the final results, which is why Figure 3.8 includes the representation of the velocity correlation using this scale. Here we see how at smaller smoothing scales, the velocity correlation function drops faster (closer to the halo center). This means that using a bigger smoothing scale will allow more of the overdensity of the two-halo contribution to be contributing to the total kSZ signal.

3.6 Halo kSZ contribution results

Finally, we turn to the kSZ integration using the previously explained model. The aim of this section is to analyse the relation between the kSZ flux coming from halos and the kSZ flux coming a larger volume of the same aperture as the halo's but larger depth along the LOS, for which it is necessary to take into account the two-halo density contribution. The latter, modulated by the velocity correlation function, will provide the amount of electrons contributing to the obtained kSZ flux.

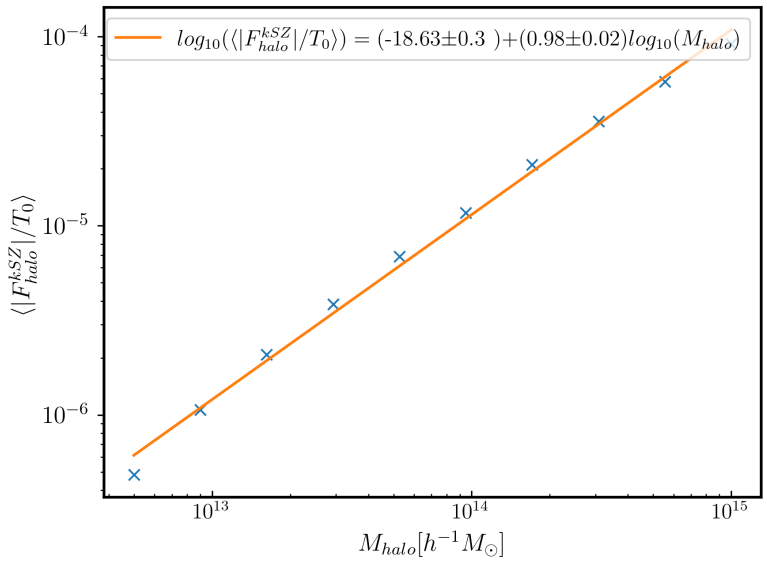

Figure 3.9: kSZ flux coming from within the halo in relation to halo mass.

The resulting equation through which we can calculate the kSZ flux in this model is

$$\langle|F^{kSZ}(z,M,R,\hat{n})|\rangle = T_{\rm CMB}\int d\Omega \int_{r_g-d/2}^{r_g+d/2} dr\ \sigma_T \overline{n}_e(r,\hat{n})(1+z)^2\sigma_v(z,R)f(r)\Delta_g^{1h+2h}(r,M)/c, \quad (3.37)$$

where the angular integral has been introduced to take into account the aperture of the integration volume, which has a radius equal to the virial radius of the halo being observed along the line of sight $\hat{n}$. The reason for making the mass halo M and the smoothing scale R separate variables is that the latter has not been always chosen in relation to the halo mass, but we may have followed simpler choices (like 30 h^{-1}Mpc). It should be noted that the semi-analytical results will be calculated for masses between $5\times10^{12}-10^{15}$ $M_\odot/h$, given the extrapolation of the one-halo overdensity from CM21 becomes unreliable outside of these bounds.
The results of the kSZ flux coming from within the halo in relation to halo mass are shown in Figure 3.9. They are linearly fit to check they are compatible with the notion of kSZ flux inside the halo being proportional to halo mass. Indeed, the results are coherent in this sense.

In Figure 3.6 one can see that there is a two halo overdensity contribution that is specially relevant at high halo masses, and which regarding the kSZ signal, is modulated by the velocity correlation function. This means the top hat window function used dictates the amount of electrons contributing to the kSZ signal when we are looking at integration distances larger than the virial radius. This is considering within the virial radius the velocity of electrons is completely correlated.
The kSZ flux coming from inside halos is intended to be compared to the kSZ flux associated to larger distances to see how the rest of the free electrons outside alter the kSZ along the LOS of the cluster. In doing so, one must make a compromise and choose a particular smoothing scale which suits the physical requirements of the problem. For instance, here we are applying linear theory and using a semi-analytical model for $z=0.1$ and masses roughly between 5×10^{12}-10^{15} $M_\odot$. The first part is the main consideration for using radii between $15-30$ h^{-1}Mpc. In Figure 3.8 these two extremes are used in obtaining the velocity correlation, so in practice it is foreseeable that greater R results in a bigger flux coming from the extended integration volumes, as more electrons are 'allowed to contribute' to the kSZ as a consequence of their radial peculiar velocities being correlated. We therefore study the impact of R in the results, comparing these using the Lagrangian radii associated to each mass, $R=15$ Mpc/h and $R=30$ Mpc/h. In Figure 3.10a results of the kSZ flux ratio between the halos and several cylinders varying in LOS depth between $d=10-512$ Mpc/h at redshift $z=0.1$ using the Lagrangian radius of each mass. In Figures 3.10b and 3.10c the results of these kSZ flux ratios has been calculated using smoothing scales $R=15$

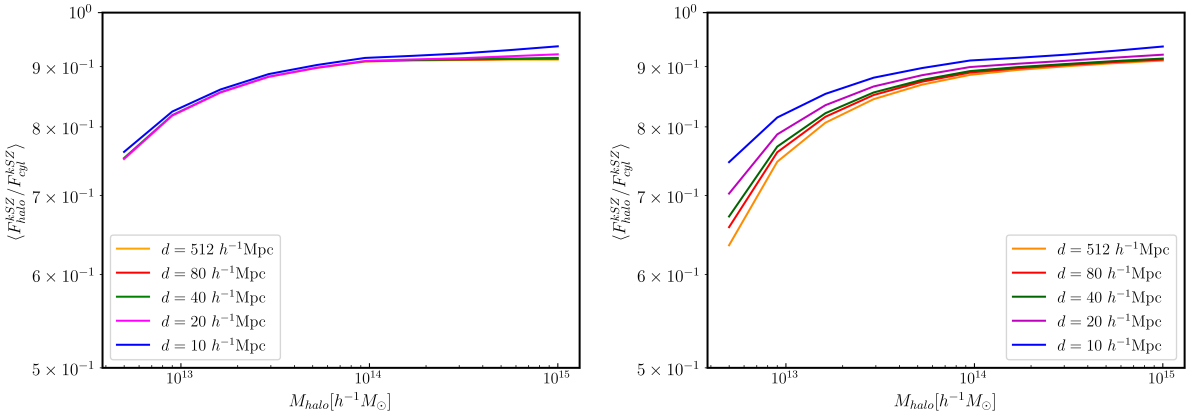

(a) $R = R_L$

(b) $R = 15$ Mpc/h

(c) $R = 30$ Mpc/h

Figure 3.10: kSZ flux ratio between halos and cylinders of depth d and same aperture as the halos, defined by the virial radius, calculated using a smoothing scale of (a) the Lagrangian radii of the halos, (b) $R = 15$ Mpc/h and (c) $R = 30$ Mpc/h.

Mpc/h and $R = 30$ Mpc/h respectively. These verify that bigger smoothing scales allow for greater kSZ free-electron contribution, specially at lower masses seen from the furthest distances considered, and also that bigger mass halos have a stronger halo contribution, which doesn't surpass 95%, regardless of R. However, it is clearly seen how this parameter affects the results, which is something to be taken into consideration, and makes one think this model would benefit from having numerical simulations against which to be compared. Applying the Lagrangian radii seems to limit the most the contribution of electrons from the two-halo overdensity to the kSZ flux.

4. Cosmological simulations methodology

Además del tratamiento semi-analítico expuesto en el anterior capítulo, se ha hecho uso de datos obtenidos con una simulación cosmológica, provistos por el Prof. Dr. Raúl Angulo, para probar la hipótesis principal con la que se comenzó este proyecto: comprobar si hay una porción de señal kSZ asociada a un cúmulo de galaxias que proviene del medio interestelar en la línea de visión, aparte de la contribución del flujo proveniente del halo, y cuantificarla en tal caso. La simulación usada por el momento solo contiene halos y partículas de materia oscura a redshift $z = 0$; no tiene en cuenta aún procesos de física bariónica. Para un subconjunto de halos del catálogo, se ha calculado el ratio entre la señal kSZ proveniente de halos y la proveniente de toda la línea de visión. También se ha estudiado el ratio del kSZ asociado a los halos en comparación con regiones de 40 y 80 h^{-1}Mpc de profundidad que abarcan y están centradas en dichos halos. Para ello, se ha aplicado a los datos de la simulación un código Python para hacer el cálculo de la señal de kSZ proveniente de los halos de materia oscura, proveniente de toda la línea de visión y también de volúmenes cilíndricos centrados en el halo de 40 y 80 h^{-1}Mpc de profundidad. En el programa se han tenido en cuenta las condiciones periódicas de contorno del catálogo de halos y partículas de materia oscura y se ha hecho una selección del $\sim 18\%$ de halos del catálogo siguiendo un criterio que no afectase gravemente a la estadística de la masa de halos. Se ha comprobado también la proporcionalidad con la masa del halo del flujo de kSZ proveniente de los halos. El promedio de los resultados se ha hecho excluyendo aquellos halos cuya señal en la línea de visión (o en los volúmenes de 40 y 80 h^{-1}Mpc) fuera $|T^{kSZ}_{LOS}| < 0.05 \cdot |T^{kSZ}_{halo}|$ (ó $|T^{kSZ}_{40Mpc}| < 0.05 \cdot |T^{kSZ}_{halo}|$), ya que se considera que el hecho de que haya cancelación de las velocidades peculiares del gas ionizado en esa región provoca que el ratio que se estudia dé valores absolutos demasiado elevados y ruidosos. Los resultados dejan ver que la contribución del gas de electrones libres (fuera del radio virial del halo) es $(45 \pm 6)\%$ para una profundidad de 512 h^{-1}Mpc, $(29 \pm 7)\%$ para una profundidad de 80 h^{-1}Mpc y $(25 \pm 3)\%$ para una profundidad de 40 h^{-1}Mpc a lo largo de la línea de visión, teniendo un crecimiento casi despreciable con la masa de los halos.

The aim of this Chapter is to set up the principal concepts underlying cosmological simulations, to explain the methodology used to analyse the free electron contribution to the kSZ with N-body simulation data, and to lay out the results obtained of the kSZ signal contribution of halos to the total kSZ signal along the LOS. The method by which the kSZ measurements have been performed using the simulation data provided by Prof. Dr. R. Angulo (DIPC) is explained in §*4.1*, while §*4.2* presents the results obtained from the kSZ temperature distortion caused by the galaxy clusters' halos in comparison to the kSZ temperature distortion seen along the whole LOS.

Cosmological simulations are a key tool for the study of LSS formation and evolution in the Universe. They have proven to be particularly useful to confront observational data from astronomical surveys with theoretical models and predictions, especially the ΛCDM paradigm. This model was shown to be quantitatively compatible with almost all LSS and smaller scale observations (Angulo and Hahn, 2022). They have also become a very relevant tool for creating mock universes from which to extract valuable information about physical processes and their observability, and to interpret the physics from the cosmological observations. This ties into their utility to measure the amount of kSZ signal coming from a certain volume in a mock version of the Universe.
These numerical simulations involve the modelling of dark energy, dark matter and baryonic matter and various physical processes such as gravity, gas cooling, feedback processes, radiation and many more. Cosmological simulations can be divided in two broad categories, dark matter N-body simulations

h [100 km s^{-1} Mpc^{-1}]	Ω_m	Ω_b	Ω_Λ	σ_8	ω_a	ω_0
0.678	0.307	0.048	0.693	0.9	0.0	-1.0

Table 4.1: Cosmological simulation parameters.

and hydrodynamical simulations. They can also be classified into zoom simulations (they resolve smaller scales and are well-suited to study galaxy formation) and large scale simulations, which provide statistical samples of galaxies. They start off from smooth initial conditions, which specify the perturbations on the homogeneous expanding background and are constrained by CMB observations, and through the set of equations governing the different Universe components yield detailed predictions of the LSS at lower redshifts than the initial redshift (typically, the density fluctuation field is specified at redshift $z \sim 100$) or lower (Vogelsberger et al., 2020). The mass distribution is usually represented by particles on a grid, with the movement of each mass element being traced numerically by taking into account the interactions with the other mass elements. Due to limitations in RAM, even in the supercomputers where these cosmological simulations are conducted, the mass element in these numerical experiments are many orders of magnitude larger that, for instance, a stellar mass, and this implies some degree of approximation, particularly on the smallest scales resolved by the simulation. Once the simulation is done, there are several algorithms that can be used to define the halos, such as the Friends-of-Friends (FoF) algorithm.

The dark matter simulations used for this project do not include baryonic matter, but, as will later be explained, shortly we will certainly be using hydrodynamical simulations, as well as simulation data corresponding to higher redshifts.

4.1 Methodology for kSZ measurements with simulations

For this method, I was able to develop a Python program to calculate the contribution to the to the total LOS kSZ signal of galaxy clusters as traced by dark matter halos in a mock universe obtained from a cosmological simulation. The N-body simulation data has been provided by Prof. Dr. R. Angulo (DIPC) in the form of a cubic parcel of $L = 512\ h^{-1}$Mpc at $z = 0$ containing $N_h = 436,707$ halos (with their respective positions, velocities and virial masses) and a $1/64$ subset from a total of $N_p = 1536^3$ dark matter particles (with corresponding positions and velocities, and a mass of $m_{particle} = 3.156 \times 10^9 h^{-1} M_\odot$).The cosmological parameters used for this simulation can be found in Table 4.1. It includes the ΛCDM critical densities for total mass, baryonic mass, and dark energy, the Hubble parameter, the amplitude of matter fluctuations σ_8, and the parameters for the equation of state of the dynamical dark energy, which are given in $\omega(z) = \omega_0 + (1+z)\omega_a$. Additionally, Figure 4.1 shows a representation using TOPCAT[1] of the spatial halo density inside the parcel.
The Python program works by isolating, for each halo, the particles inside the three following volumes:

- A sphere of radius the halo's virial radius, R_{200}.
- A cylinder with the same depth as the parcel, 512 h^{-1}Mpc, and aperture radius R_{200}.
- Cylinders of smaller depth (40 h^{-1}Mpc, 80 h^{-1}Mpc) centred on the halo and with an aperture radius R_{200}.

The equation used to calculate the kSZ flux [2]from the particles inside the halo is

$$\frac{F_{halo}^{kSZ}}{F_{\rm CMB}} = -\frac{\sigma_T}{\pi R_v^2} \sum_{i=1}^{N_{part}} N_{ep} \frac{v_{z,i}}{c} \tag{4.1}$$

[1]http://www.star.bris.ac.uk/ mbt/topcat/
[2]Note that we are computing kSZ fluxes provided we are integrating the brightness temperature over the solid angle subtended by the halo.

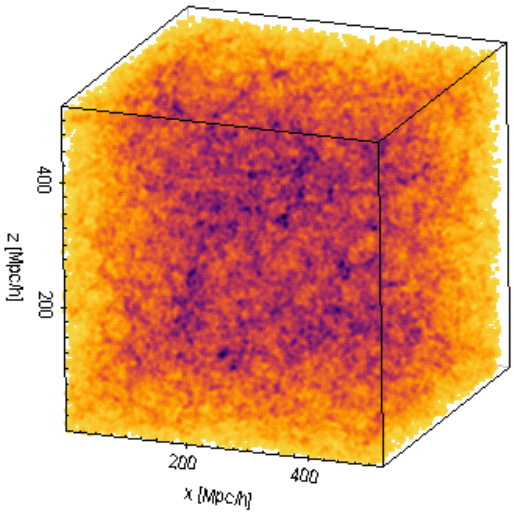

Figure 4.1: Halo density in the simulation cubic box at redshift $z = 0$.

where v_z are the particle's corresponding velocities along the LOS, which has been chosen to correspond to the z axis, R_v is the virial radius and N_{ep} is the number of electrons inside a dark matter particle,

$$N_{ep} = M_{part} \frac{\Omega_b}{\Omega_m} f_{gas} \frac{1}{\mu m_p}, \tag{4.2}$$

with μ the molecular weight of the gas and f_{gas} the fraction of baryonic matter in the form of gas. The kSZ flux coming from the LOS and the shorter cylinders is calculated similarly, only in Eq.(4.1) the number of particles would be the one corresponding to those search volumes, hence it is their velocities which would have to be used as well. The aperture radius remains being the virial radius of the halo.
It should be mentioned that the simulation data parcel has periodic boundary conditions, which were successfully taken into account in the Python program so the selection of particles inside the mentioned search volumes was valid and no particles were left out when it surpassed any of the parcel boundaries. Periodic boundary conditions are often used in cosmological simulations, as they provide a gateway to escape aliasing effects when computing spatial Fourier transforms. Several preliminary runs of the code, using a small amount of halos of assorted virial masses, confirmed that the Virial Theorem held for the particles inside the halo, and that the mass of the particles inside the halos corresponded to the known mass of the halos (see Appendix B). This indicated that the selection of particles was being made correctly.
Lastly, not all the halos in the catalogue were used due to the time-consuming code runs, instead, a compromise was made in such a way that the subset of halos didn't suppose a considerable bias to the relevant halo statistics. The used mass binning is represented in Figure 4.2 and it shows the number of halos inside each of the 15 mass bins. Concerning the initial halo mass distribution, the smaller mass bins ($< 10^{13}\ h^{-1} M_\odot$) had a great deal more of halos than the higher mass bins, which is why a maximum of 10000 randomly chosen halos was established for lower mass bins. This means a total of 76916 halos were used for this analysis, which is 17.6% of the number of halos in the catalogue.

4.2 kSZ results from simulations

The simulation results for the kSZ signal coming from the halos as a function of their mass are depicted in Figure 4.3, along with the mean calculated inside of each mass bin. They include a linear fit made in logarithmic scale which shows the relation between the kSZ signal and the cluster mass, which indicates $\langle F_{halo}^{kSZ}/T_0 \rangle \propto M_{halo}^{1.17 \pm 0.13}$. This fits coherently into the picture we had of the fact that the LOS component of the velocity isn't dependent on the halo mass and F_{halo}^{kSZ}/T_0 should be dependent on the halo mass, as was also found in the semi-analytic result (see Figure 3.9). The kSZ flux magnitude is also

in accordance with what was expected for these halo mass values.

The kSZ LOS and cylinder ratios obtained with the previously explained method gave some surprising results due to the existence of very high absolute values ($|F^{kSZ}_{halo}/F^{kSZ}_{LOS}| > 1000$), which biased the average of each of the 15 bins. These extreme values indicate that in some cases the peculiar velocity field along the bigger volumes suffered from cancellation, which is what makes the halo contribution stand out so much. The preliminary results using all the data are found in Appendix B, where they are portrayed along with the median for the 15 bins. These results are quite noisy but already point to the kSZ contribution from unbound electrons being $20-30\%$ of the total kSZ signal. This contribution seems to be higher, $\sim 40\%$, for lower mass halos seen along the whole LOS in the simulation box. The free-electron contribution also seems to be slightly lower the bigger the halo mass, although in each of the observed depths the increase with halo mass, as portrayed by the slope of the linear fitting, is very limited.
In an effort to prescind from the extreme values, we decided to cut off those for which $|F^{kSZ}_{LOS}| < 0.05 \times |F^{kSZ}_{halo}|$ in the case of the entire LOS, and similarly for those with the 40 and 80 Mpc cylinders. The simulation results for the kSZ contribution ratios with this cut-off values are shown in Figures 4.4 and 4.5. In Figure 4.4 we can see how at low masses ($< 10^{13}\ h^{-1}M_\odot$) the kSZ signal contribution coming from unbound electrons is around $45-50\%$ of the total kSZ observed along the LOS, and at medium masses ($< 5\cdot 10^{14}\ h^{-1}M_\odot$) it is about $30-40\%$. At higher masses, results have higher errors due to the low high-mass halo statistics (see Figure 4.2), and they oscillate around an 20% kSZ contribution from free electrons, except the penultimate average, which surpasses unity value. The last value doesn't have an error bar, as there was only one halo in the last mass bin.

For the 80 $h^{-1}M_\odot$ deep cylinders centred in the halos (see Figure 4.5a), the kSZ signal contribution from free electrons stays at about $(29 \pm 7)\%$, except for the two averages before last, which are the subject of a bigger noise ratio. It makes sense, however, that the contribution coming from electrons bound in the halo is bigger (the free electron contribution smaller) than in the case of the LOS. The LOS is 512 h^{-1}Mpc deep, which means there is a bigger quantity of free electrons that is contributing to the kSZ if the LOS peculiar velocity correlation allows for such long-range contribution. Plus, there may also be electrons in the LOS which are not bound to the observed galaxy cluster, but to another galaxy cluster in radial proximity to the LOS, which also contribute to the kSZ signal. This reasoning is also in agreement with the results in the 40 h^{-1}Mpc cylinder in Figure 4.5b, where we see the halo contribution is slightly higher and the free electron contribution is at $(25 \pm 3)\%$. It has similar values at high masses to those of the 80 h^{-1}Mpc deep cylinder.
The linear fitting performed seem to be better suited for the smaller size cylinders, as for the entire LOS, the relation between the kSZ ratio and the halo mass seems less linear, specially at smaller halo masses. The increase of the ratio with halo mass is very small as well in all cases, undetectably increasing towards unity at higher masses. The low high-mass halo statistics may be partly responsible for this, as we are incapable of particularly gauging how much this affects the results.

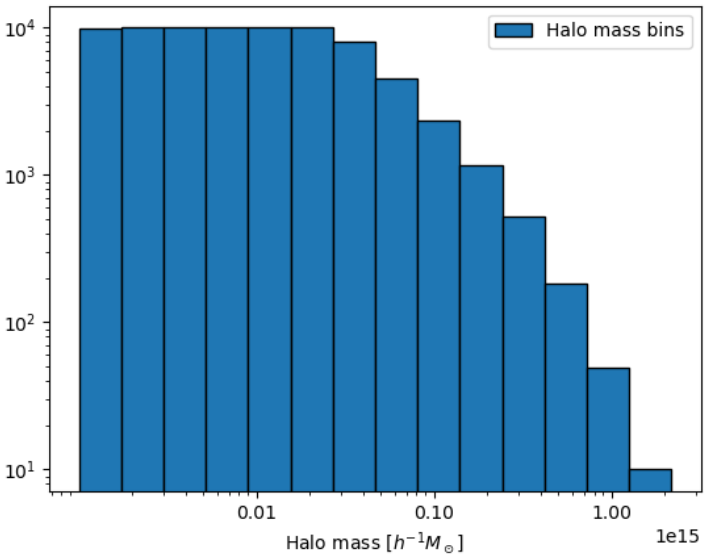

Figure 4.2: Histogram with 15 equally-spaced logarithmic halo mass bins. A maximum of 10^4 randomly chosen halos has been fixed, which affects the lower mass bins, as they are the most populated.

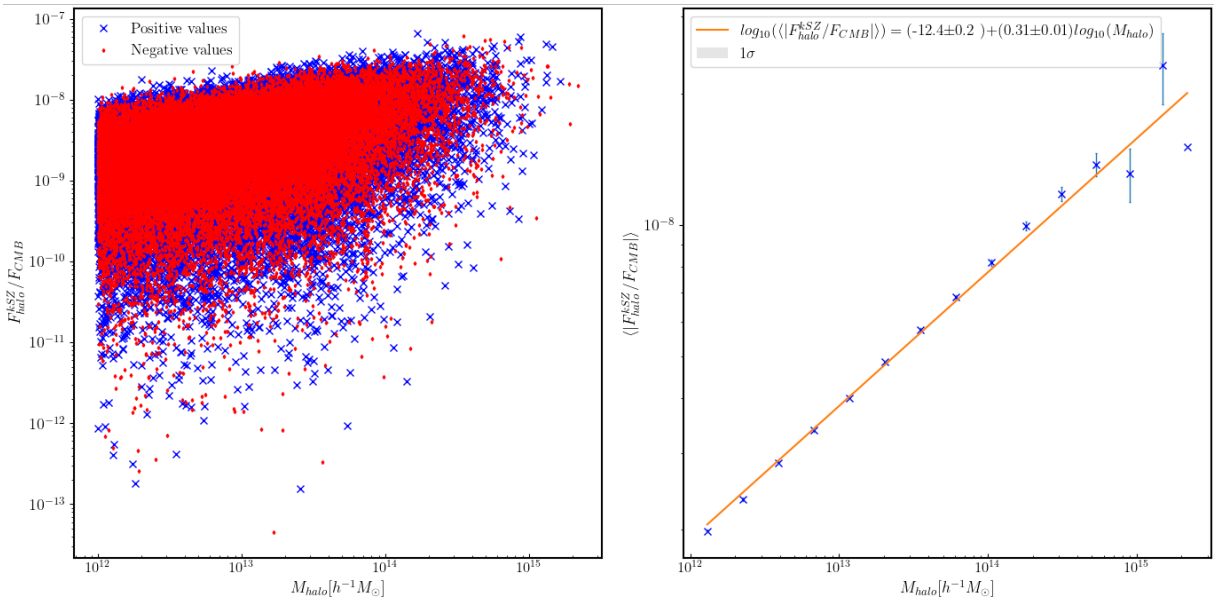

Figure 4.3: kSZ-induced flux coming from the subset of halos in the simulation (left-hand panel) and the mean for each of the 15 bins. The linear fit performed depicts the dependence of the kSZ distortion caused by the halo with the halo mass.

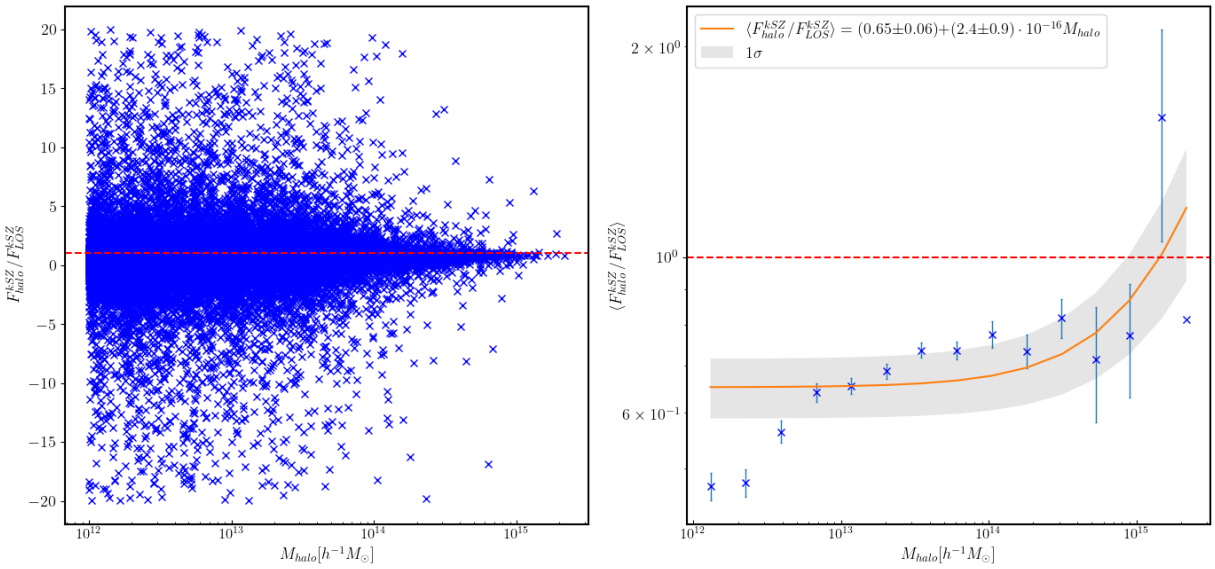

Figure 4.4: Simulation results of the ratio of flux coming from the galaxy halos,F^{kSZ}_{halo}, and the kSZ flux coming from the LOS of the halo, F^{kSZ}_{LOS}. Results shown in the left-hand panel are without averaging and exclude those cases in which $|F^{kSZ}_{LOS}| < 0.05 \cdot |F^{kSZ}_{halo}|$. The right-hand panel shows the averaged data in 15 equally spaced mass bins along with the linear fit performed, and a red dashed line signalling the ratio unity.

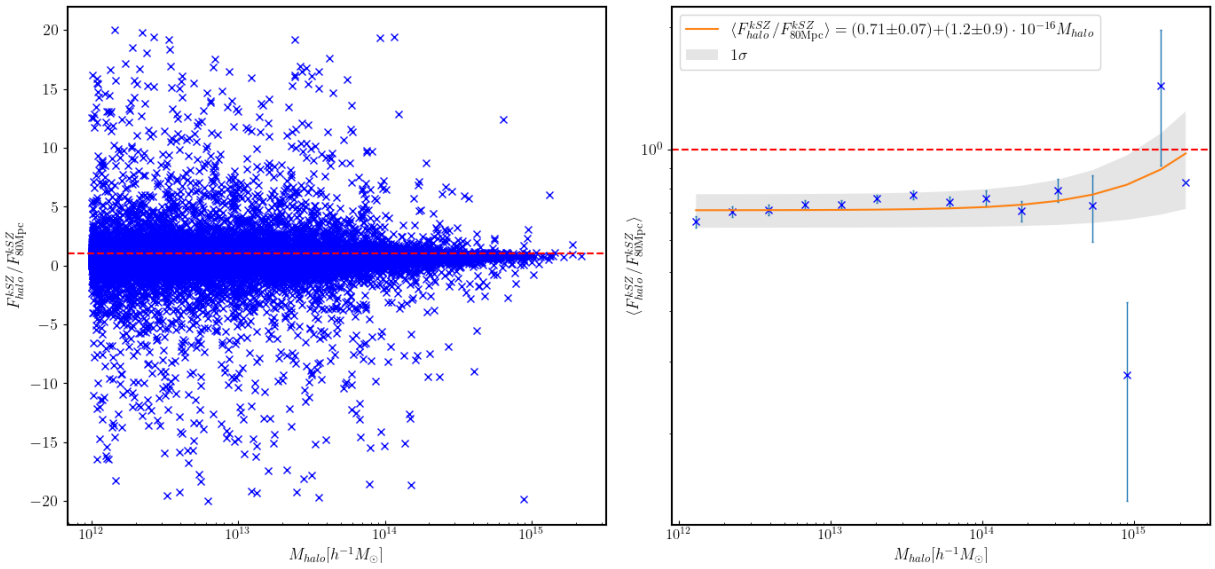

(a) kSZ flux ratio using 80 h^{-1}Mpc deep cylinders.

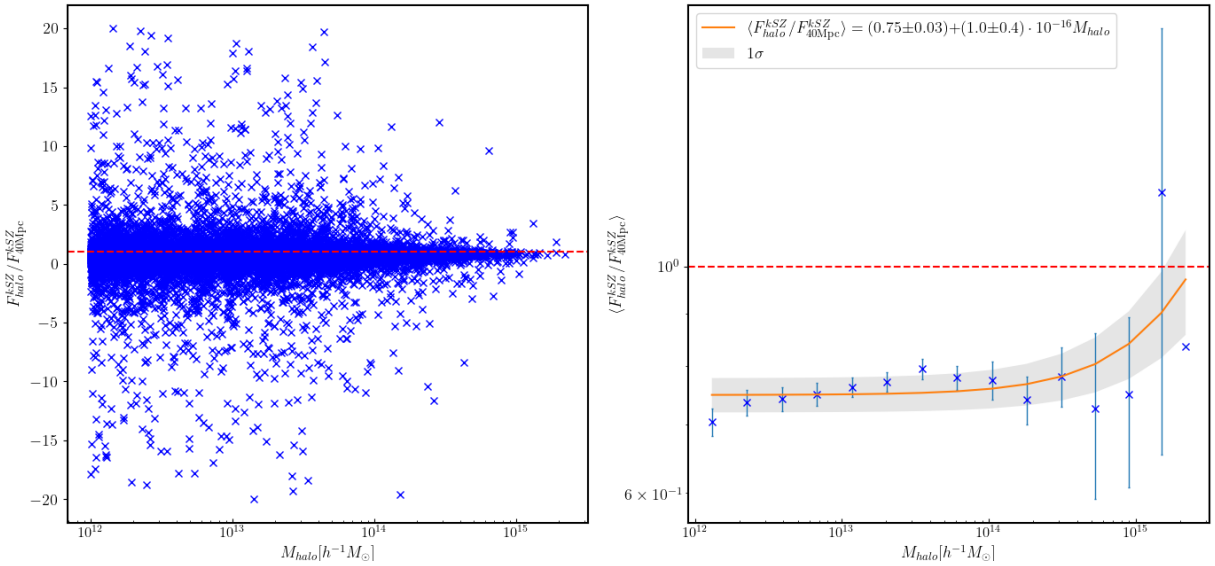

(b) kSZ flux ratio using 40 h^{-1}Mpc deep cylinders.

Figure 4.5: Simulation results of the ratio of kSZ flux coming from the galaxy halos and the kSZ flux coming from the (a)80 and (b)40 h^{-1}Mpc cylinders centred in the halo with aperture radius the virial radius of the halo. Results shown in the left-hand panel are without averaging and exclude those cases in which $|F^{kSZ}_{cyl}| < 0.05 \cdot |F^{kSZ}_{halo}|$. The right-hand panel shows the averaged data in 15 equally spaced mass bins along with the linear fits performed, and a red dashed line signalling the ratio unity.

5. Discussion of results

Los resultados del modelo semi-analítico y los obtenidos mediante los datos de la simulación cosmológica pueden ser estudiados por separado y comparándolos a redshift $z \sim 0$. Los resultados del flujo de kSZ proveniente únicamente de los halos por ambos modelos son compatibles entre sí, tanto en magnitud como en dependencia con la masa de los halos. En el caso de los ratios, los del modelo semianalítico están afectados por el radio escogido de la función ventana, ya que a escalas mayores de este, mayor es la distancia a la que está la mitad del factor de correlación de las velocidades (ver Figura 3.8), lo cuál aumenta el número de electrones fuera del halo (la contribución a dos halos) que contribuyen a la señal de kSZ. Al compararlos con los resultados de simulación vemos que comparan mejor cuando el rango de la función ventana es de $R = 15$ Mpc que con rangos menores (los radios Lagrangianos de los halos), aunque la forma de la curva es similar usando estos. Aunque no son del todo coherentes entre sí, es cierto que apuntan a que hay una contribución a tener en cuenta de electrones fuera del radio virial de los cúmulos de galaxias que contribuyen a la señal de kSZ. Ésta varía dependiendo de la distancia al halo y de la masa de este. En ambos modelos, es para los halos más masivos ($\gtrsim 10^{15} M_\odot/h$) cuando tenemos las menores contribuciones al flujo de kSZ por parte de electrones libres ($5 - 10\%$), debido a que predomina la contribución proveniente del halo, mientras que se encuentra que para halos de baja masa esta contribución es mayor ($30 - 50\%$).
La diferencia entre el modo en que los resultados analíticos y los resultados con la simulación dependen con la masa del halo se debe, en parte, a que los datos de la simulación proporcionada por Prof. Dr. Raúl Angulo no tienen materia bariónica mientras que los de la simulación usada en el artículo Chaves-Montero et al., 2021, sí tienen en cuenta procesos de física bariónica. No obstante, esta influencia se debería ver más claramente a bajas masas que a masas intermedias.

In this chapter we proceed to analyse and compare the results obtained by the semi-analytical model and the numerical simulation method. Starting by the results of the semi-analytical model, where we saw the impact of cylinder depth and mass on the ratio between halo and cylinder kSZ flux. These results are more limited with respect to halo mass than the simulation results, as can be seen in Figure 5.1, due to the extrapolation of the overdensity profiles from CM21 becoming unreliable outside of the range $5 \times 10^{12} - 10^{15}\ M_\odot/h$. It should also be noted that in order to have a more coherent comparison between methods, we took into account that the length of the simulation box (512 h^{-1}Mpc) meant the lower limit of integration for k would have to be $k_{min} = 2\pi/L_{box} = 2\pi/512(h^{-1}\text{Mpc}) \sim 10^{-2}\ h/\text{Mpc}$.

Depending on the smoothing scale R, the ratio between halo and cylinder kSZ flux has different magnitudes at the same redshift and for the same mass. A bigger smoothing scale allowed for more free electrons to contribute to the cylinder kSZ, as it makes the correlation function drop at larger distances from the halo center. Because the choice of smoothing scale is rather arbitrary, we hold side by side these results with those of the simulation to see how they compare using different smoothing scales. By studying the results in Figure 5.1 we see that greater smoothing scales are a better fit to the simulation results than the Lagrangian radii, although for middle masses they still fit poorly. We notice this when the analytical results for the halo contribution grow between 2×10^{13} and $\sim 10^{14}\ M_\odot/h$ and then they reach a plateau, while the simulation results remain almost constant, except for the case of the 512 Mpc/h deep cylinders, where it is clear that for low masses the halo contribution dips and it slightly rises at the highest masses. This difference of results between models is not so surprising when taking into consideration the fact that, while Prof. Dr. Rául Angulo's simulation data did not contain baryonic matter, the simulation used to obtain the 1-halo overdensity profiles in CM21, did in fact take into account baryonic physics. What is still puzzling, and is also something I am currently working on, is the fact that,

while one expects the baryonic effects to affect mostly the lower mass halos, it is the intermediate-mass halos which show the greatest discrepancy between both methods'results. For the moment, it is apparent that the semi-analytical ratio results for the 512 Mpc/h deep cylinder using $R \simeq 15$ Mpc/h are the most compatible with the simulation results.
One could say the overall results are, however, clear as to the existence of a free-electron contribution to the kSZ flux which is most notable for lower halo masses ($\sim 45\%$ for $M_{halo} \lesssim 10^{13} M_{\odot}/h$), which decreases with mass to $\lesssim 10\%$ for $M_{halo} \gtrsim 10^{15} M_{\odot}/h$. This means the free-electron mass associated to the kSZ contributions along the LOS would, in case of the ratio being 40% for 10^{13} $M_{\odot}/h$, be 4×10^{12} $M_{\odot}$, which would be less than the mass associated to the kSZ contribution for the case in which the ratio is $\sim 10\%$ for 10^{15} $M_{\odot}/h$, where the free electron mass would be 10^{14} $M_{\odot}/h$. This has to do with the most massive halos in the simulation being in the densest regions of the simulation, part of the so called 'nodes' in the simulation, whereas the least massive halos are typically surrounded by a less-denser region.

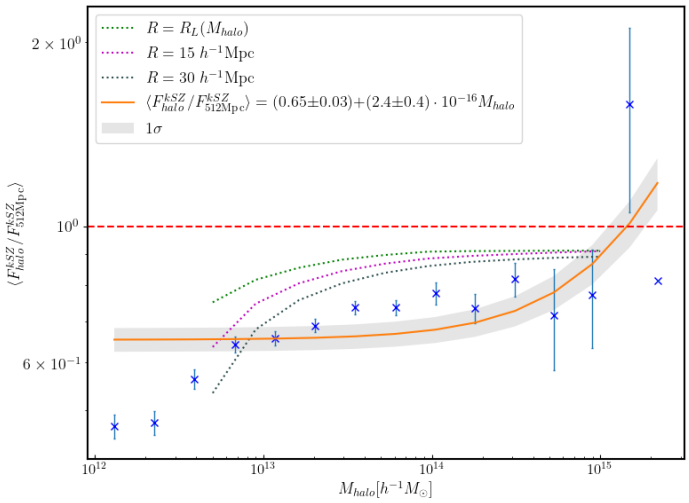

(a)

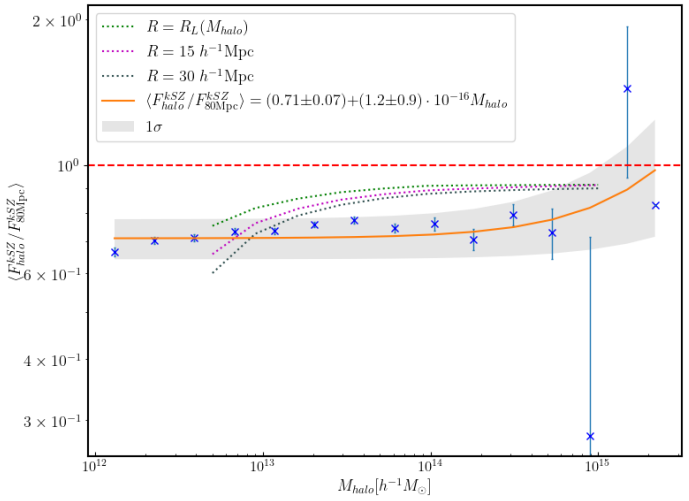

(b)

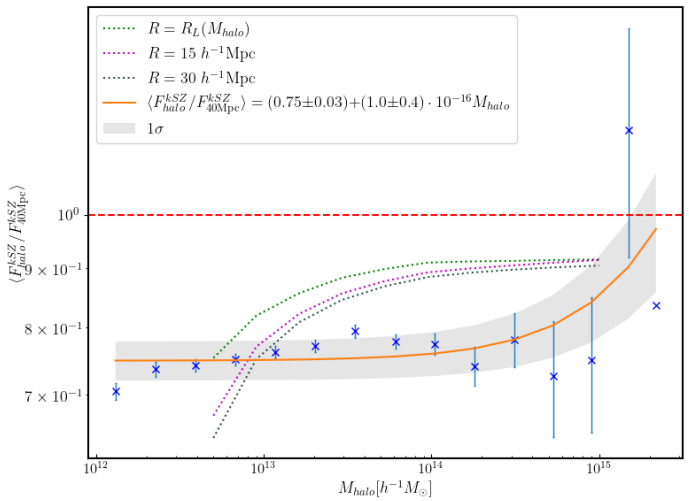

(c)

Figure 5.1: Comparison of semi-analytic and simulation results for cylinders with aperture radius the virial radius of the cluster and depth (a) 512, (b) 80 and (c) 40 Mpc/h.

6. Conclusions and future work

En este trabajo se ha comprobado, por medio de los resultados tanto del modelo semi-analítico como con simulación numérica de materia oscura, que existe una contribución del gas de electrones fuera del radio virial del halo que contribuye al flujo de kSZ a lo largo de la línea de visión correspondiente a un cúmulo de galaxias. Esta contribución es más importante en el caso de halos de baja masa, donde oscila entre el $30 - 40\%$, que para halos de grandes masas, donde no obstante sigue siendo del $5 - 10\%$ del flujo total de kSZ. Esto hace que las mediciones de masa de cúmulos de galaxias a través de este efecto sobreestimen, en mayor o menor cantidad dependiendo de la masa del cúmulo y su entorno, la masa en caso de que no se llegue a tener en cuenta la contribución del gas libre de electrones a la señal de kSZ. En el futuro próximo se planea trabajar con diferentes *snapshots* de la simulación a distintos redshifts para ver cómo varía la contribución al kSZ de los electrones libres con este parámetro. También se trabajará con una simulación que incluya materia bariónica además de materia oscura, la cual permitirá estudiar el efecto de la subestructra de los cúmulos y el impacto del gas expulsado por procesos de la física bariónica.

The conclusions drawn from this work can be summed up by stating that the obtained results give a clear indication that there is a free-electron contribution to kSZ fluxes which may cause an overestimation of the galaxy cluster mass measurements, specially for those with masses $\leq 10^{13}\ h^{-1}M_{\odot}$. Using the linear theory approach involving theoretical modelling and numerical simulations, we have found this contribution to be greater in absolute magnitude for lower mass halos ($\sim 40\%$ for halo masses between $10^{12} - 10^{13}\ h^{-1}M_{\odot}$) than for the highest masses ($\sim 10\%$ for halo masses $\gtrsim 10^{15}\ h^{-1}M_{\odot}$). Additionally, we have found evidence for the unbound contribution to stabilize at the $30 - 40\%$ level at depths larger than 80 Mpc/h. Although the dependence on mass of the free-electron contribution is not the same for the two methods, this could be explained by the fact that the simulation data extracted by Prof. Dr. Raúl Angulo did not contain baryonic matter while the simulation used by CM21 did. However, this is unprobable since baryons should affect mostly low mass halos, and the different behaviour affects practically all mass ranges.

The fact that the results from the simulation display a rather flat versus mass behaviour in the halo ratio seems counter-intuitive, and seemingly in contradiction with the results from the semi-analytical model. The latter results appear more natural, although even a perfectly flat ratio could be explained by an increasing density in the environment of more massive halos. This is currently being the subject of dedicated exploration. As for the future work concerning this topic, I plan on using other snapshots of the simulation at different redshifts to study how the kSZ free-electron contribution varies with it, and using simulation data with baryonic matter to better compare with the theoretical results. In this case, I foresee having to make changes to the methodology used for this project, as inclusion of baryons will reveal a different matter distribution, now with subhalos and galaxies within the dark matter halos. Various snapshots at different redshifts will also be used in this scenario. I will also try to get better results by using more powerful computational resources and to somehow compensate the low high-mass halo statistics.

Bibliography

Angulo, R. E., & Hahn, O. (2022). Large-scale dark matter simulations. *Living Reviews in Computational Astrophysics*, *8*(1). https://doi.org/10.1007/s41115-021-00013-z

Calafut, V., Gallardo, P. A., Vavagiakis, E. M., Amodeo, S., Aiola, S., Austermann, J. E., Battaglia, N., Battistelli, E. S., Beall, J. A., Bean, R., Bond, J. R., Calabrese, E., Choi, S. K., Cothard, N. F., Devlin, M. J., Duell, C. J., Duff, S. M., Duivenvoorden, A. J., Dunkley, J., … Xu, Z. (2021). The Atacama Cosmology Telescope: Detection of the pairwise kinematic Sunyaev-Zel'dovich effect with SDSS DR15 galaxies., *104*(4), Article 043502, 043502. https://doi.org/10.1103/PhysRevD.104.043502

Carlstrom, J. E., Holder, G. P., & Reese, E. D. (2002). Cosmology with the Sunyaev-Zel'dovich Effect., *40*, 643–680. https://doi.org/10.1146/annurev.astro.40.060401.093803

Cen, R., & Ostriker, J. P. (1999). Where Are the Baryons?, *514*(1), 1–6. https://doi.org/10.1086/306949

Chaves-Montero, J., Hernández-Monteagudo, C., Angulo, R. E., & Emberson, J. D. (2021). Measuring the evolution of intergalactic gas from z = 0 to 5 using the kinematic Sunyaev-Zel'dovich effect., *503*(2), 1798–1814. https://doi.org/10.1093/mnras/staa3782

Douspis, M. (2011). Planck sz clusters, 21–26.

Emberson, J. D., Frontiere, N., Habib, S., Heitmann, K., Larsen, P., Finkel, H., & Pope, A. (2019). The borg cube simulation: Cosmological hydrodynamics with CRK-SPH. *The Astrophysical Journal*, *877*(2), 85. https://doi.org/10.3847/1538-4357/ab1b31

ESA. (2019). *Hunting Galaxy Clusters with Planck – The Sunyaev-Zel'dovich Effect*. https://sci.esa.int/web/planck/-/53104-cosmic-structure

Fukugita, M., Hogan, C. J., & Peebles, P. J. E. (1998). The Cosmic Baryon Budget., *503*(2), 518–530. https://doi.org/10.1086/306025

Hernández-Monteagudo, C., Ma, Y.-Z., Kitaura, F. S., Wang, W., Génova-Santos, R., Macıas-Pérez, J., & Herranz, D. (2015). Evidence of the missing baryons from the kinematic sunyaev-zeldovich effect in planck data. *Phys. Rev. Lett.*, *115*, 191301. https://doi.org/10.1103/PhysRevLett.115.191301

Hernández-Monteagudo, C., Verde, L., Jimenez, R., & Spergel, D. N. (2006). Correlation Properties of the Kinematic Sunyaev-Zel'dovich Effect and Implications for Dark Energy., *643*(2), 598–615. https://doi.org/10.1086/503190

Kravtsov, A. V., & Borgani, S. (2012). Formation of galaxy clusters. *Annual Review of Astronomy and Astrophysics*, *50*(1), 353–409. https://doi.org/10.1146/annurev-astro-081811-125502

Lewis, A., & Challinor, A. (2011). CAMB: Code for Anisotropies in the Microwave Background.

Mather, J. C., Cheng, E. S., Cottingham, D. A., Eplee, J., R. E., Fixsen, D. J., Hewagama, T., Isaacman, R. B., Jensen, K. A., Meyer, S. S., Noerdlinger, P. D., Read, S. M., Rosen, L. P., Shafer, R. A., Wright, E. L., Bennett, C. L., Boggess, N. W., Hauser, M. G., Kelsall, T., Moseley, J., S. H., … Wilkinson, D. T. (1994). Measurement of the Cosmic Microwave Background Spectrum by the COBE FIRAS Instrument., *420*, 439. https://doi.org/10.1086/173574

Mo, H., van den Bosch, F. C., & White, S. (2010). *Galaxy Formation and Evolution*.

Nicastro, F., Kaastra, J., Krongold, Y., Borgani, S., Branchini, E., Cen, R., Dadina, M., Danforth, C. W., Elvis, M., Fiore, F., Gupta, A., Mathur, S., Mayya, D., Paerels, F., Piro, L., Rosa-Gonzalez, D., Schaye, J., Shull, J. M., Torres-Zafra, J., … Zappacosta, L. (2018). Observations of the missing baryons in the warm–hot intergalactic medium. *Nature*, *558*(7710), 406–409. https://doi.org/10.1038/s41586-018-0204-1

Ondaro-Mallea, L., Angulo, R. E., Zennaro, M., Contreras, S., & Aricò, G. (2022). Non-universality of the mass function: dependence on the growth rate and power spectrum shape., *509*(4), 6077–6090. https://doi.org/10.1093/mnras/stab3337

Persic, M., & Salucci, P. (1992). The baryon content of the Universe. *Monthly Notices of the Royal Astronomical Society*, *258*(1), 14P–18P. https://doi.org/10.1093/mnras/258.1.14P

Planelles, S., Schleicher, D. R. G., & Bykov, A. M. (2015). Large-Scale Structure Formation: From the First Non-linear Objects to Massive Galaxy Clusters., *188*(1-4), 93–139. https://doi.org/10.1007/s11214-014-0045-7

Press, W. H., & Schechter, P. (1974). Formation of Galaxies and Clusters of Galaxies by Self-Similar Gravitational Condensation., *187*, 425–438. https://doi.org/10.1086/152650

Rees, M. J., & Sciama, D. W. (1968). Large-scale Density Inhomogeneities in the Universe., *217*(5128), 511–516. https://doi.org/10.1038/217511a0

Sachs, R. K., & Wolfe, A. M. (1967). Perturbations of a Cosmological Model and Angular Variations of the Microwave Background., *147*, 73. https://doi.org/10.1086/148982

Seljak, U. (1996). Gravitational lensing effect on cosmic microwave background anisotropies: A power spectrum approach. *The Astrophysical Journal*, *463*, 1. https://doi.org/10.1086/177218

Shull, J. M., Smith, B. D., & Danforth, C. W. (2012). THE BARYON CENSUS IN a MULTIPHASE INTERGALACTIC MEDIUM: 30% OF THE BARYONS MAY STILL BE MISSING. *The Astrophysical Journal*, *759*(1), 23. https://doi.org/10.1088/0004-637x/759/1/23

Sunyaev, R. A., & Zeldovich, Y. B. (1970). The Spectrum of Primordial Radiation, its Distortions and their Significance. *Comments on Astrophysics and Space Physics*, *2*, 66.

Sunyaev, R. A., & Zeldovich, Y. B. (1972). The Observations of Relic Radiation as a Test of the Nature of X-Ray Radiation from the Clusters of Galaxies. *Comments on Astrophysics and Space Physics*, *4*, 173.

Tinker, J. L., Robertson, B. E., Kravtsov, A. V., Klypin, A., Warren, M. S., Yepes, G., & Gottlöber, S. (2010). The Large-scale Bias of Dark Matter Halos: Numerical Calibration and Model Tests., *724*(2), 878–886. https://doi.org/10.1088/0004-637X/724/2/878

Vavagiakis, E. M., Gallardo, P. A., Calafut, V., Amodeo, S., Aiola, S., Austermann, J. E., Battaglia, N., Battistelli, E. S., Beall, J. A., Bean, R., Bond, J. R., Calabrese, E., Choi, S. K., Cothard, N. F., Devlin, M. J., Duell, C. J., Duff, S. M., Duivenvoorden, A. J., Dunkley, J., … Xu, Z. (2021). The Atacama Cosmology Telescope: Probing the baryon content of SDSS DR15 galaxies with the thermal and kinematic Sunyaev-Zel'dovich effects., *104*(4), Article 043503, 043503. https://doi.org/10.1103/PhysRevD.104.043503

Vogelsberger, M., Marinacci, F., Torrey, P., & Puchwein, E. (2020). Cosmological simulations of galaxy formation. *Nature Reviews Physics*, *2*(1), 42–66. https://doi.org/10.1038/s42254-019-0127-2

Weinberg, D. H., Miralda-Escudé, J., Hernquist, L., & Katz, N. (1997). A Lower Bound on the Cosmic Baryon Density., *490*(2), 564–570. https://doi.org/10.1086/304893

A. Halo corrected overdensity profiles

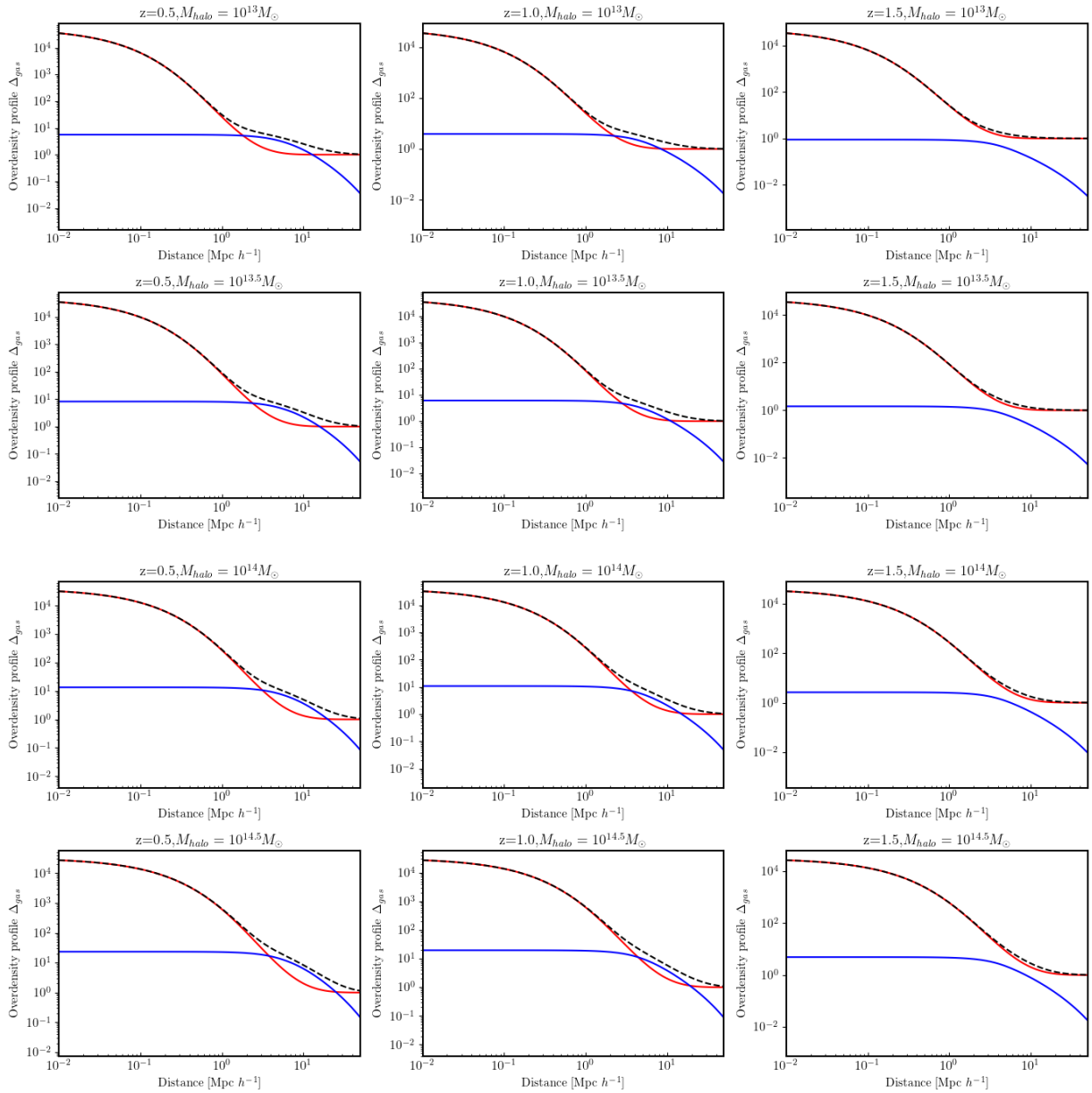

Figure A.1: Halo-density corrected overdensity profiles for four halo masses at redshifts z=0.5,1,1.5. Red solid lines show original profiles from CM21, or the 1 halo term, adjusted through double exponential fit, blue solid line shows 2 halo term as a function of the distance to the halo center, and black dashed lines is the sum of both contributions, which is the total Δ_{gas}.

B. First simulation results

The particle selection algorithm was checked in the case of the halos by comparing the number of particles selected in the halo (inside a sphere of virial radius) times their mass and comparing that to the known halo mass. The results are portrayed in Figure B.1a, where we can see that, although at lower masses they're more poorly defined, the average is unity independently of the halo mass. Figure B.1b shows the rms velocity of the particles inside the halos, which, seeing that $v_{rms} \propto M_{halo}^{1/3}$, is in accordance with the Virial Theorem.

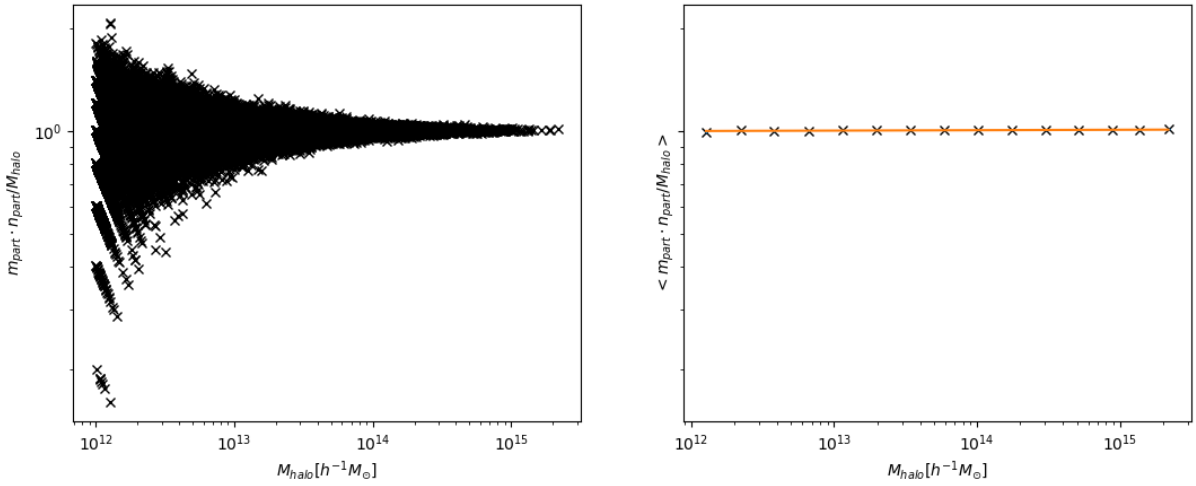

(a) Mass ratio of selected particles inside a halo and known halo mass.

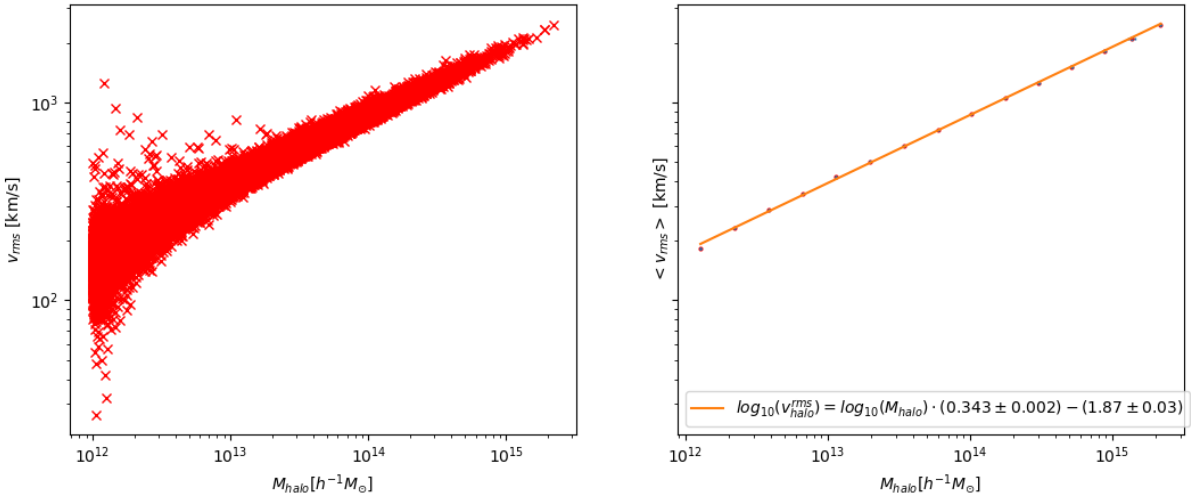

(b) Root mean square velocity of selected particles inside halos as a function of mass, aimed at checking the Virial Theorem.

Figure B.1: Preliminary checks to see if the particle selection algorithm was valid.

The results obtained from the simulations of the kSZ ratio between contributions first included those in which the larger volume in the ratio suffered from peculiar velocity cancellation, which lead to very large values of the ratio. Here are those results, with the median calculated for 15 mass bins.

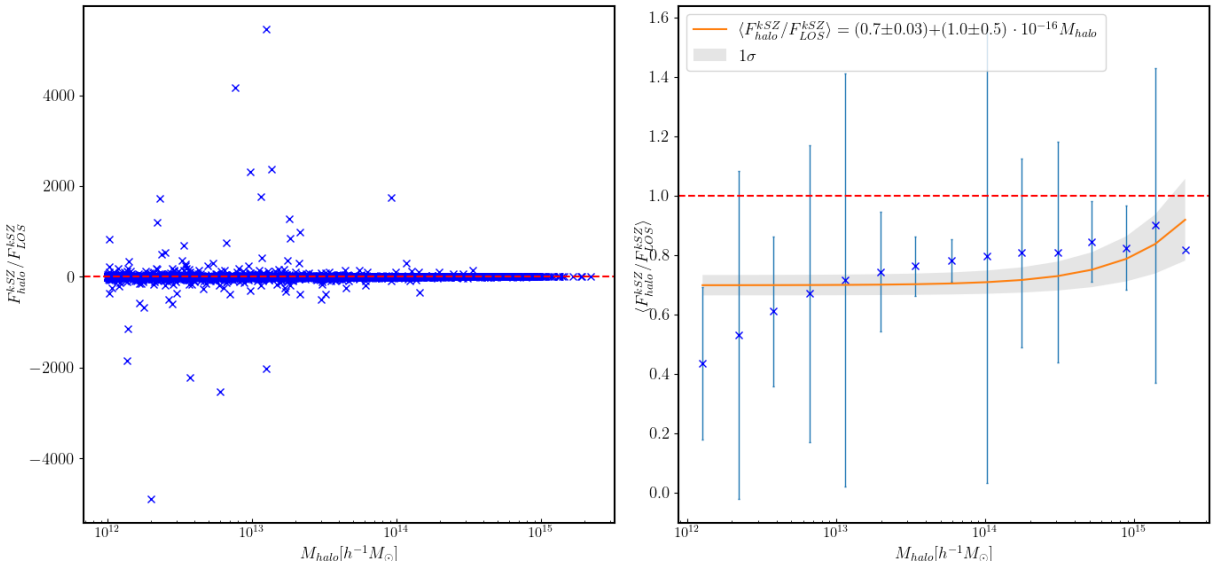

Figure B.2: Simulation results of the ratio of signal coming from the galaxy halos,T^{kSZ}_{halo}, and the kSZ signal coming from the LOS of the halo, T^{kSZ}_{LOS}. Results shown in the left-hand panel are without averaging. The right-hand panel shows the median in 15 equally spaced mass bins along with the linear fit performed, and a red dashed line signalling the ratio unity.

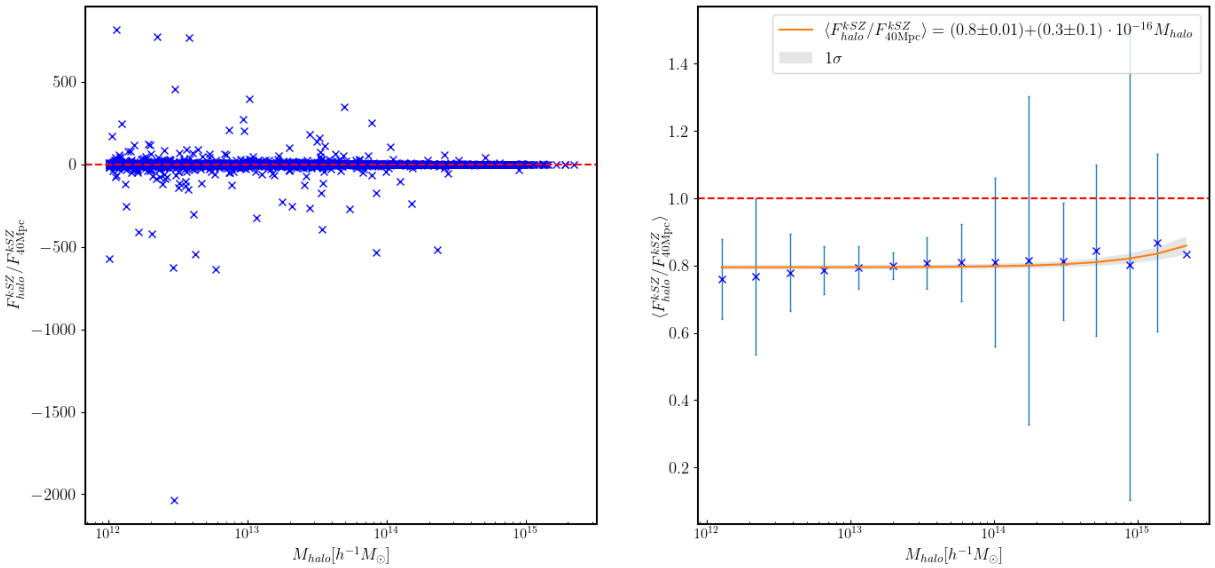

(a) kSZ signal ratio using 80 h^{-1}Mpc deep cylinders.

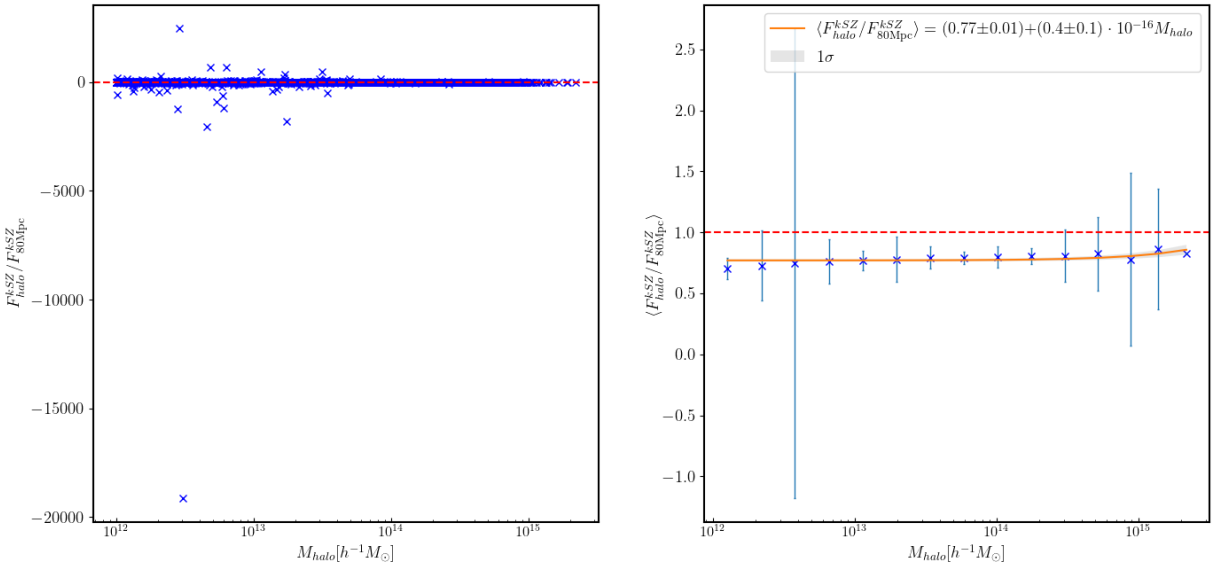

(b) kSZ signal ratio using 40 h^{-1}Mpc deep cylinders.

Figure B.3: Simulation results of the ratio of kSZ signal coming from the galaxy halos and the kSZ signal coming from the (a)80 and (b)40 h^{-1}Mpc cylinders centered in the halo with aperture radius the virial radius of the halo. Results shown in the left-hand panel are without averaging. The right-hand panel shows the median in 15 equally spaced mass bins along with the linear fits performed, and a red dashed line signalling the ratio unity.